JCB Journal of Cell Biology

ARTICLE

A conserved myotubularin-related phosphatase regulates autophagy by maintaining autophagic flux

Elizabeth A. Allen[1], Clelia Amato[2], Tina M. Fortier[1], Panagiotis Velentzas[1], Will Wood[2], and Eric H. Baehrecke[1]

Macroautophagy (autophagy) targets cytoplasmic cargoes to the lysosome for degradation. Like all vesicle trafficking, autophagy relies on phosphoinositide identity, concentration, and localization to execute multiple steps in this catabolic process. Here, we screen for phosphoinositide phosphatases that influence autophagy in *Drosophila* and identify *CG3530*. CG3530 is homologous to the human MTMR6 subfamily of myotubularin-related 3-phosphatases, and therefore, we named it dMtmr6. dMtmr6, which is required for development and viability in *Drosophila*, functions as a regulator of autophagic flux in multiple *Drosophila* cell types. The MTMR6 family member *MTMR8* has a similar function in autophagy of higher animal cells. Decreased *dMtmr6* and *MTMR8* function results in autophagic vesicle accumulation and influences endolysosomal homeostasis.

Introduction

Cells rely on macroautophagy (hereafter autophagy) to deliver sequestered cytoplasmic cargoes to lysosomes for degradation. Basal autophagy levels maintain cellular homeostasis, and activated autophagy mitigates several cellular stresses, including nutrient deprivation. Autophagy begins with the formation of an isolation membrane that elongates and encloses cargoes to eventually form a closed double-membrane autophagosome that fuses with lysosomes to become an autolysosome (Yu et al., 2018). Lysosomal enzymes, including cathepsins, break down autophagic cargoes into macromolecules, which are later effluxed into the cytoplasm for use in anabolic cellular processes. Pioneering yeast experiments defined the core autophagic molecular mechanisms (Tsukada and Ohsumi, 1993). However, metazoans such as *Drosophila melanogaster* possess an enhanced repertoire of autophagic machinery beyond those required in yeast, thus providing a multicellular in vivo experimental system to study autophagy (Mulakkal et al., 2014; Zhang and Baehrecke, 2015).

From initiation to completion, autophagy is regulated by >30 conserved core autophagy-related (Atg/ATG) proteins (Galluzzi et al., 2017). Autophagy initiation and autophagosome biogenesis require the Atg1–ULK1 serine–threonine kinase complex, the vacuolar protein sorting (Vps34) class III phosphoinositide (PI) 3-kinase (PI3K) complex, and the Atg8 conjugation system. Autophagosome–lysosome fusion utilizes dozens of proteins, including many shared with the endocytic pathway and the autophagosomal SNARE protein Syntaxin 17 (Takáts et al., 2013; Itakura et al., 2012). When lysosomal enzymes complete autophagic cargo degradation, then autolysosome reformation contributes to regeneration of the lysosomal pool, which further promotes homeostasis (Yu et al., 2010). Both excessive and insufficient autophagy can promote disease by dysregulating autophagic flux, a term that describes the quantity of autophagic degradation (Dowling et al., 2015; Levine and Kroemer, 2019; Yoshii and Mizushima, 2017), making rate control a key component to each step of autophagy.

Vesicular membrane identity and trafficking rely largely upon PI identity, concentration, and coincidence (Schink et al., 2016). PI kinases (PIKs) and phosphatases can switch the 3-, 4-, and 5-hydroxyl group phosphates of the inositol ring to generate seven distinct cellular PIs. Membrane-embedded PIs recruit effectors to control membrane dynamics via multiple mechanisms, including membrane fusion, scission, and shaping. In the endolysosomal system, PI(3)P is the major PI species on endosomes following PI conversion from PI(4,5)P_2, which is required for endocytosis (Wallroth and Haucke, 2018). Recycling endosomes rely on a PI(3)P loss (Campa et al., 2018) and PI(4)P gain (Ketel et al., 2016), while degradative PI(3)P-positive endosomes require PI(3,5)P_2 production by the PI(3)P 5-kinase PIKFYVE for endosomal sorting complexes required for transport (ESCRT)-III recruitment and delivery to multivesicular bodies (Kim et al., 2014; Hasegawa et al., 2017). Similar PI conversion events occur

[1]Department of Molecular, Cell, and Cancer Biology, University of Massachusetts Medical School, Worcester, MA; [2]Centre for Inflammation Research, The Queen's Medical Research Institute, University of Edinburgh, Edinburgh, UK.

Correspondence to Eric H. Baehrecke: eric.baehrecke@umassmed.edu.

during uptake and degradation of either extracellular fluids or particles by macropinocytosis or phagocytosis, respectively (Zoncu et al., 2009), and phagosome maturation coincides with PI(3)P reduction (Levin et al., 2015). Likewise, autophagy progression from start to finish relies upon PI identity changes. Autophagy initiation requires recruitment of the class III PI3K complex I to preautophagosomal structures (Funderburk et al., 2010), which results in PI(3)P production and recruitment of autophagosome-forming effectors (Lystad and Simonsen, 2016). Meanwhile, autophagosome–lysosome fusion requires multiple PI conversion events. For example, fusion requires production of PI(4)P at autophagosomes by PIK4IIα (Wang et al., 2015), as well as lysosomal PI(3,5)P_2 synthesis by PIKFYVE (de Lartigue et al., 2009) and hydrolysis by INPP5E (Hasegawa et al., 2016). After fusion, a transient PIP5K-mediated PI(4,5)P_2 increase on the lysosomal surface recruits clathrin machinery (Rong et al., 2012), which is followed by inositol polyphosphate-5-phosphatase (OCRL)-mediated PI(4,5)P_2 turnover to PI(4)P for autophagic lysosome reformation (De Leo et al., 2016).

Both PI(3)P and PI(3,5)P_2 facilitate degradative membrane-driven cellular processes. Thus, as described above, enzymes that catalyze their synthesis or turnover play critical roles in trafficking membrane-bound cargoes to the lysosome. Myotubularin-related phosphatases (MTMRs) are a conserved family of 3-PI phosphatases that are associated with diseases (Raess et al., 2017) and regulate membrane trafficking during endocytosis and autophagy (Nicot and Laporte, 2008; Robinson and Dixon, 2006). Of the 16 human MTMRs, 9 contain the catalytically active CX_5R motif, and 7 are catalytically dead pseudophosphatases due to a cysteine residue substitution. The MTMR family of enzymes are grouped into subfamilies, and the *Drosophila* genome harbors a single orthologue in each subfamily. One human MTMR subfamily consists of human MTMR6, MTMR7, and MTMR8. These all partner with MTMR9, an inactive pseudophosphatase that fails to bind PIs on its own (Zou et al., 2012b) but enhances substrate binding, catalytic activity, and protein stability of its active partners in vitro and in cells (Zou et al., 2009a, 2012b).

Here, we identify *CG3530/dMtmr6* as a regulator of autophagy in *Drosophila*. We reveal that dMtmr6, which is homologous to the human MTMR6 subfamily of myotubularin-related 3-phosphatases, functions as an essential regulator of autophagic flux in multiple cell types and is required for *Drosophila* development. Down-regulation of *dMtmr6* leads to autophagic vesicle accumulation, promotes lysosome biogenesis, and impairs both endocytosis and phagocytosis. Importantly, we show that MTMR8 has similar function in autophagy in higher animal cells. This work establishes dMtmr6 as an essential regulator of autophagic flux.

Results

Drosophila CG3530/dMtmr6 negatively regulates Atg8a puncta formation and is essential for survival and development

Enzymes that regulate autophagy represent potential drug targets for human disorders (Rubinsztein et al., 2012), and cycles of phosphorylation and dephosphorylation provide regulatory cues for autophagy and other cellular processes. However, the phosphatases that regulate autophagy remain largely unexplored. We sought to identify novel phosphatases that regulate autophagy by screening the *Drosophila* PI phosphatases because of their links to membrane trafficking and autophagy. We used the flippase/flippase-recognition target (FLP/FRT) system (Golic and Lindquist, 1989; Theodosiou and Xu, 1998) to simultaneously express GFP and RNAi that target phosphatases in clones of cells within tissues that uniformly express the autophagy reporter mCherry-Atg8a.

Drosophila larval intestine enterocytes contain pmCherry-Atg8a puncta 2 h after puparium formation (APF) due to high levels of developmental autophagy (Denton et al., 2009). Therefore, we evaluated the effects of PI phosphatase RNAi on mCherry-Atg8a expression in 2-h-APF midguts (Table S1). We identified multiple previously described regulators of autophagy, such as PTEN (not shown), as well as *CG3530/Mtmr6* (*dMtmr6* hereafter), a previously undescribed regulator of autophagy. Expression of double-stranded RNA targeting *dMtmr6* generates cells that contain Atg8a puncta in feeding third-instar larvae (L3) when autophagy remains inactive in neighboring WT cells (Fig. 1, A and B). At 2 h APF, *dMtmr6*-knockdown enterocytes contain both increased and enlarged mCherry-Atg8a puncta compared with neighboring WT cells (Fig. 1, B–D).

We sought to determine if *dMtmr6* regulates autophagy either specifically in larval intestine developmental autophagy or more broadly in multiple cell contexts, including stress-induced autophagy following nutrient deprivation. Therefore, we investigated if *dMtmr6* functions in amino acid starvation–induced autophagy in the *Drosophila* larval fat body (Scott et al., 2004). We examined fat body tissue from either fed L3 that lack autophagy or animals grown on 20% sucrose under nutrient-restriction conditions for 4 h to induce autophagy. As in midguts of the intestine, *dMtmr6*-knockdown fat body cells contain Atg8a puncta in fed larvae, and Atg8a puncta are significantly larger in *dMtmr6*-knockdown cells than in adjacent WT cells from starved larvae (Fig. 1, E–H). These data indicate that *dMtmr6* functions in both developmental and starvation-induced autophagy in *Drosophila*.

To better understand the function of *dMtmr6*, we deleted the *dMtmr6* open reading frame using CRISPR-Cas9 (Fig. 2 A). Knockdown of *dMtmr6* in all tissues using both strong and weak RNAi strains results in lethality at either the early larval stage or early pupal stage, respectively (Fig. 2 B). Importantly, homozygous loss of *dMtmr6* (*dMtmr6Δ/Δ*) is larval lethal, as is *dMtmr6Δ/Df* (Fig. 2 B). However, some trans-heterozygous mutant animals (*dMtmr6Δ/dMtmr6*^{KG01267}) survive until adult stage. *dMtmr6*^{KG01267} is a mutant allele made by P-element insertion in the 5′ UTR of the *dMtmr6* B and C isoforms, but not A (Fig. 2 A), which suggests that the P-element insertion is a weak allele. To evaluate the effects of *dMtmr6* loss on autophagy, we measured protein levels from whole larvae (feeding L3). Trans-heterozygous *dMtmr6Δ/KG* and *dMtmr6Δ/Df* animals have increased levels of the cargo receptor ref(2)p (p62 in mammals) and lipidated Atg8a compared with control heterozygous animals lacking one allele of either the null *dMtmr6Δ* or weak allele *dMtmr6* ^{KG01267} (Fig. 2, C–C″). We then used

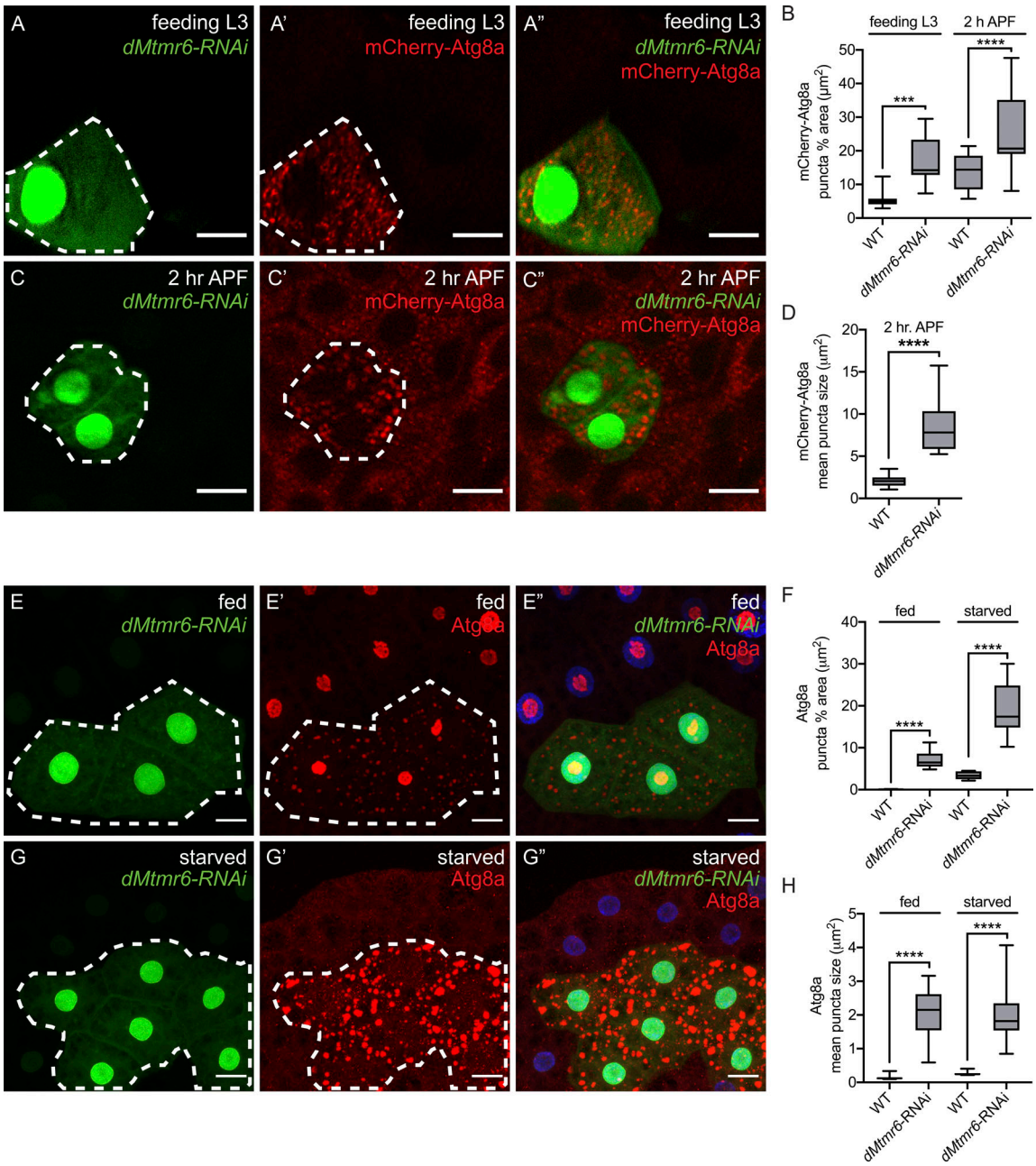

Figure 1. ***Drosophila* CG3530/dMtmr6 negatively regulates Atg8a puncta formation. (A)** Control (GFP-negative) and d*Mtmr6*-knockdown cells (white dotted line, green) from midguts expressing pmCherry-Atg8a during the feeding L3 stage. **(B)** Quantification of pmCherry-Atg8a puncta levels in WT control cells and d*Mtmr6*-knockdown cells of midguts from feeding L3 and 2 h APF pupae. **(C)** Control (GFP-negative) and d*Mtmr6*-knockdown cells (white dotted line, green) from midguts expressing pmCherry-Atg8a during developmental autophagy (bottom) occurring 2 h APF. **(D)** Quantification of pmCherry-Atg8a puncta size in WT and d*Mtmr6*-knockdown cells from 2 h APF midguts. **(E)** Larval *Drosophila* fat body with control (GFP-negative) and d*Mtmr6*-knockdown cells (white dotted line, green) stained with an antibody to detect Atg8a and Hoechst to detect nuclei (blue) from fed animals. **(F)** Quantification of percentage of cellular area occupied by Atg8a puncta in WT and d*Mtmr6*-knockdown cells of L3 fat body from fed or starved animals as represented in E and G. **(G)** Larval *Drosophila* fat body with control (GFP-negative) and d*Mtmr6*-knockdown cells (white dotted line, green) stained with an antibody to detect Atg8a and Hoechst to detect nuclei (blue) from starved animals. **(H)** Quantification of Atg8a puncta size in WT and d*Mtmr6*-knockdown cells of L3 fat body from fed or starved animals as represented in E and G. Data in B, D, F, and H are presented as mean ± minimum to maximum ($n \geq 10$). Asterisks denote statistical significance (***, $P < 0.001$; ****, $P < 0.0001$) using paired, two-tailed *t* test. Scale bars, 20 µm.

the FLP/FRT system to generate homozygous *dMtmr6*-null mutant cell clones within WT tissue. As with *dMtmr6*-RNAi, *dMtmr6* knockout results in increased amounts of Atg8a in feeding larval midguts (Fig. 2, D and D′). However, we obtain significantly fewer *dMtmr6*Δ-null mutant cell clones than control cell clones in both the midgut and fat body (Fig. 2 E), suggesting that homozygous loss of *dMtmr6*Δ compromises cell viability. These data suggest that *dMtmr6* regulates autophagy and is critical for *Drosophila* development and that at least in some contexts, *dMtmr6* is required for cell viability.

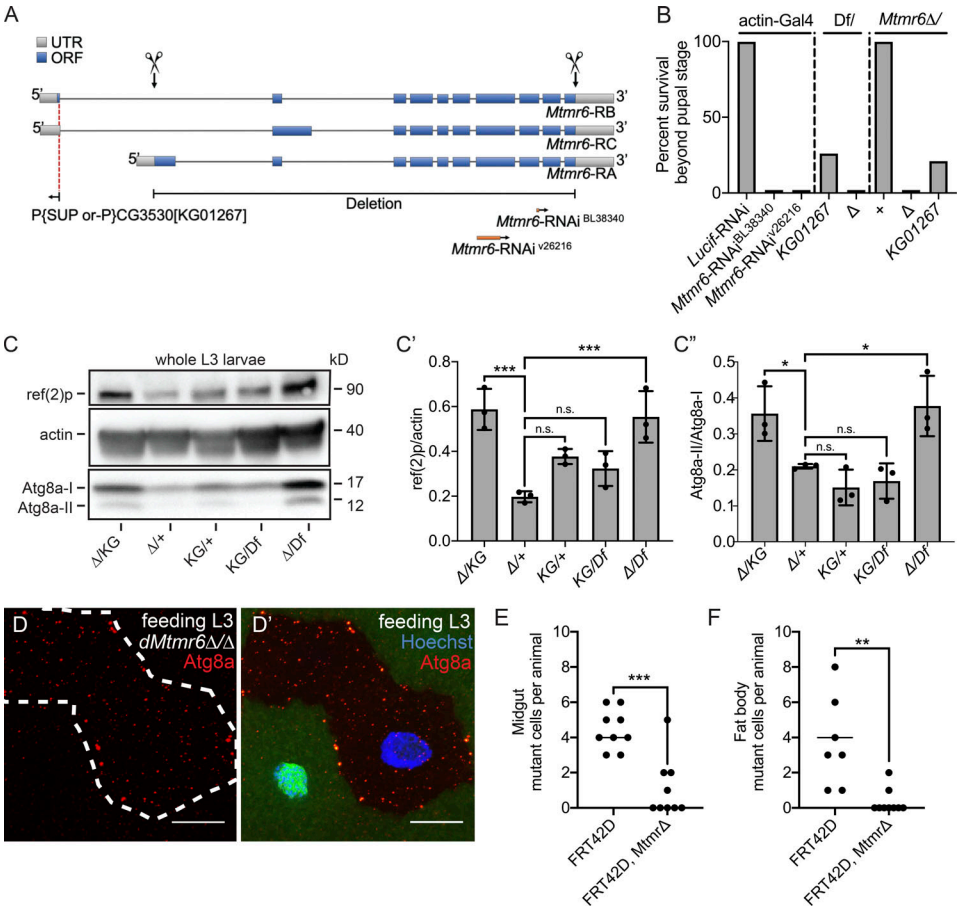

Figure 2. ***dMtmr6* is essential for development and survival. (A)** Schematic representation of *CG3530/dMtmr6*. Vertical arrows indicate the CRISPR-targeted sites and the resulting deletion. Horizontal arrows indicate P-element insertion site and RNAi target sites. **(B)** Quantification of the percentage of animals that survive beyond the pupal stage from ubiquitous knockdown experiments (left) or mutant analyses (right). **(C)** Western blot from whole larvae (feeding L3) and quantifications of the ratio of ref(2)p to actin (C′) and lipidated Atg8a-II to cytosolic Atg8a-I (C″) from the indicated genotypes. **(D)** Feeding L3 midguts with *dMtmr6*-null clone cells (white dashed outline, GFP negative) within WT tissue (green) stained with antibody to detect Atg8a and Hoechst to detect nuclei (blue). **(E)** Quantification of the number of control (FRT42D, +/FRT42D, +) and mutant (FRT42D, *dMtmr6Δ*/FRT42D, *dMtmr6Δ*) clone cells generated in midgut (left) and fat body (right) from whole larvae (feeding L3). Data are presented as percentage of $n > 100$ animals from three experimental replicates (B); mean ± SD, $n = 2$ animals, three experimental replicates (C); and individual values, $n \geq 3$ animals, three experimental replicates (E). Asterisks denote statistical significance (*, $P < 0.05$; **, $P < 0.01$; ***, $P < 0.001$), using one-way ANOVA (C) and paired, two-tailed *t* test (E and F). Scale bars, 20 µm. n.s., not significant.

dMtmr6 and mammalian MTMR8 influence autophagic flux and endolysosomal homeostasis

Our data indicate that dMtmr6 influences autophagic flux, but it is unclear at what stage flux is altered because increased Atg8a puncta could result from elevated levels of autophagic membrane biogenesis, impaired degradation, or both. We analyzed *Drosophila* fat body tissue stained with antibody to detect the autophagy cargo adapter ref(2)p to determine if lysosomal degradation of autophagic cargoes is impaired when we down-regulate *dMtmr6*. Under normal conditions, ref(2)p is internalized within the autophagosome and degraded by the autolysosome. In *dMtmr6*-knockdown fat body cells, ref(2)p levels increase compared with neighboring WT cells from fed and starved animals (Fig. 3, A–C). In addition, *dMtmr6*-knockdown cells contain larger ref(2)p spots than WT cells from starved animals (Fig. 3 D). These findings indicate that *dMtmr6* influences the rate of autophagy at the stage of initiation, degradation, or both.

dMtmr6 is an MTMR protein that is most similar to the human MTMR6 subfamily, which includes MTMR6 (65% similar, 47% identical), MTMR7 (64% similar, 47% identical), and MTMR8 (72% similar, 55% identical; Fig. 3 E and Fig. S1). The predicted catalytic domain of dMtmr6 and each of the human MTMR6-subfamily members is conserved (Fig. 3 E). However, a key difference between fly and human is that *dMtmr6* encodes an N-terminal FYVE domain, while members of the human MTMR6-subfamily encode a coiled-coil domain (Fig. 3 F). Previous studies suggest a negative role for human MTMR8 in autophagy and for MTMR6 in apoptosis (Zou et al., 2009a, 2012b). However, these studies focus on biochemical aspects of MTMR8, MTMR6, and their inactive binding partner, MTMR9, and provide very little information about how MTMR8 could function in autophagy. We transfected both COS-7 and HeLa cells with siRNA to down-regulate either *MTMR6* or *MTMR8* and confirmed a role for *MTMR8* in autophagy in primate cells. As shown

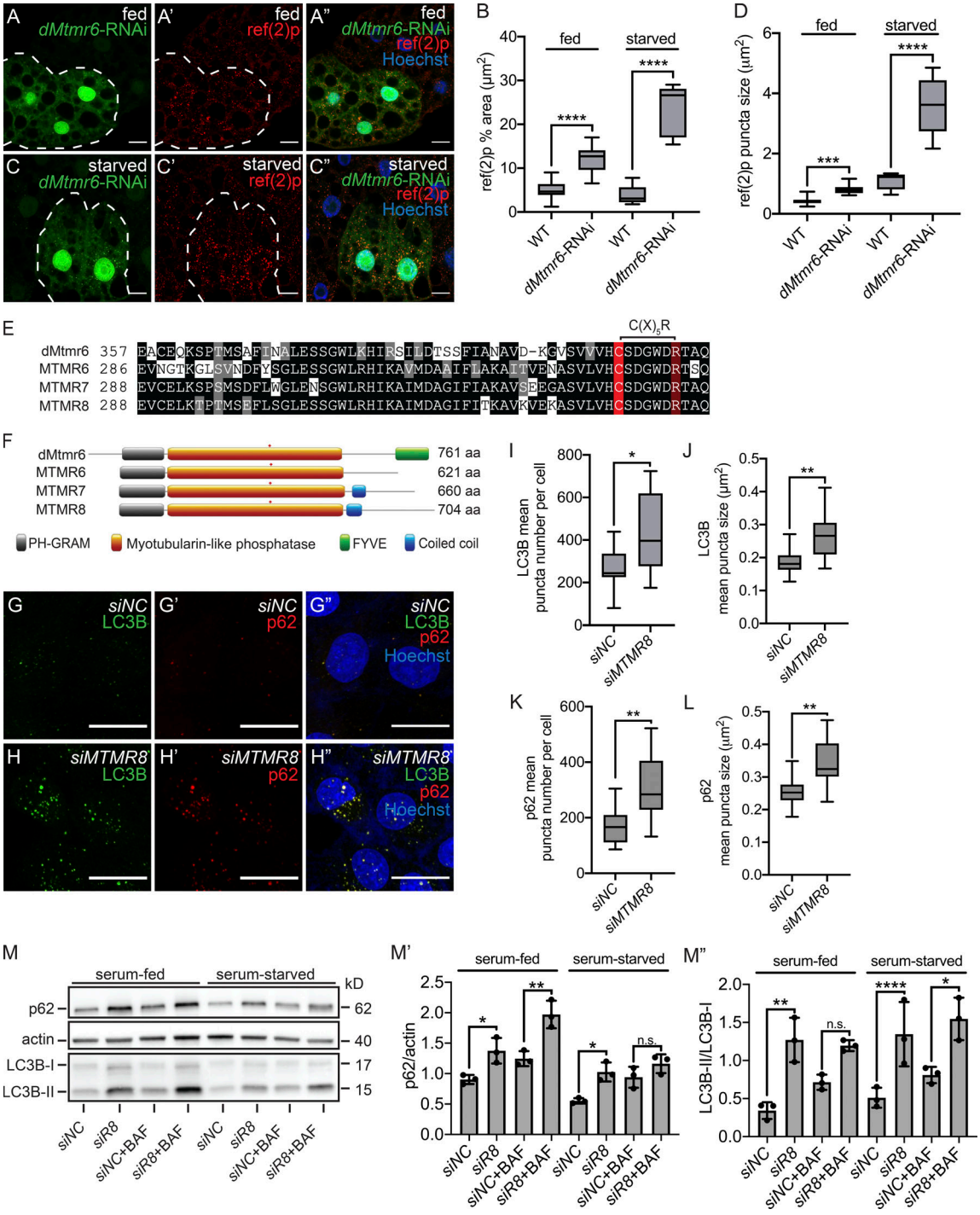

Figure 3. **dMtmr6, and the mammalian orthologue MTMR8, influence autophagic flux (A)** Representative image of fed L3 fat body with control (GFP-negative) and d*Mtmr6*-knockdown cells (white dashed outline, green cells) stained with an antibody to detect ref(2)p and Hoechst to detect nuclei (blue). **(B)** Quantification of the percentage of cellular area occupied by ref(2)p in control and d*Mtmr6*-knockdown cells of L3 fat body from fed and starved animals (shown in A and C). **(C)** Representative image of starved L3 fat body with control (GFP-negative) and d*Mtmr6*-knockdown cells (white dashed outline, green cells) stained with an antibody to detect ref(2)p and Hoechst to detect nuclei (blue). **(D)** Quantification of ref(2)p puncta size in control and *dMtmr6*-knockdown cells of L3 fat body from fed and starved animals (shown in A and C). **(E)** Amino acid sequence alignment of the CG3530, MTMR6, MTMR7, and MTMR8 catalytic domain (see Fig. S1 for full sequence alignment). **(F)** Schematic of the MTMR6 subfamily. *Drosophila* CG3530 contains an N-terminal FYVE domain. MTMR6, MTMR7, and MTMR8 contain a N-terminal coiled coil domain. **(G and H)** Representative maximum intensity projection of z-stack image from serum-fed Cos7 cells treated with scrambled siRNA (*NC*, top) or MTMR8-siRNA (bottom). Cells were stained with Hoechst (blue) to detect nuclei and antibodies to detect p62 (red) and LC3B (green). **(I–L)** Quantification of the size and number of cellular p62 and LC3B puncta as represented in G and H. **(M)** Western blot from serum-fed or serum-starved COS7 cells treated without or with Bafilomycin A1, which disrupts autophagosome-lysosome fusion, with quantification of the ratio of p62 to actin (M′) and LC3B-II to LC3B-I (M″). Data are presented as mean ± minimum to maximum, $n = 10$ each (B and D); and mean ± minimum to maximum ($n = 12$ images, three experimental replicates; I–L). Asterisks denote statistical significance (*, $P < 0.05$; **, $P < 0.01$; ***, $P < 0.001$; ****, $P < 0.0001$), using paired two-tailed *t* test (B and D), unpaired two-tailed *t* test (I–L), and one-way ANOVA (M). Scale bars, 20 μm.

previously (Zou et al., 2009a), *MTMR6* knockdown promotes HeLa cell death, but, unexpectedly, *MTMR6* knockdown in COS-7 cells did not influence viability (data not shown). Like *dMtmr6* knockdown, down-regulation of *MTMR8* produces increased numbers of large LC3B puncta in COS-7 cells (Fig. 3, G–J). Recruitment of ubiquitinated cargoes to autophagic membranes requires the autophagy adapter molecule p62 (*Drosophila* ref(2)p). Importantly, reduced *MTMR8* function resulted in increased numbers of large p62 puncta in COS-7 cells (Fig. 3, G, H, K, and L) and HeLa cells (not shown). We also observed increased lipidated-LC3B (LC3B-II) and p62 protein levels in *MTMR8* siRNA–transfected COS-7 cells in both serum-fed and serum-deprived conditions (Fig. 3, M–M″), which suggests that MTMR8-depleted cells can respond to nutrient deprivation. Furthermore, the inhibition of lysosomal function by addition of Bafilomycin A1 caused a further increase in LC3B-II and p62 levels (Fig. 3, M–M″), which supports our hypothesis that *MTMR8* inactivation impairs autophagic flux. Similar to what we observed in *Drosophila*, we hypothesize that *MTMR8* may also regulate the rate of either autophagosome biogenesis or lysosomal degradation of cargoes in higher organisms.

Genes whose molecular products facilitate autophagic flux are expressed through transcription factor EB (TFEB; *Drosophila* Mitf) mediated transcription. When inactive TFEB remains in the cytoplasm, but in response to starvation or during lysosome dysfunction, TFEB translocates to the nucleus to promote expression of both lysosome and autophagy genes (Napolitano and Ballabio, 2016). We hypothesized that if *MTMR8* inactivation impairs lysosome function, then we should see evidence of TFEB activation in *MTMR8*-depleted cells. Indeed, we detected more TFEB in the nucleus of serum-starved than serum-fed control HeLa cells, while *MTMR8*-depleted cells displayed nuclear TFEB in both serum-starved and serum-fed conditions (Fig. S2, A–E). If MTMR8 and dMtmr6 function as orthologues, then *dMtmr6* knockdown should produce activation of the *Drosophila* TFEB orthologue, Mitf. As expected, known gene targets of Mitf increased in *Drosophila* fat body *dMtmr6*-knockdown compared with control (*Lucif-RNAi*; Fig. S2 F). Despite nutrient availability, TFEB activation occurs in cells and tissues depleted of *MTMR8* or *dMtmr6*. These results suggest that inactivation of either MTMR8 or dMtmr6 may elicit lysosome dysfunction.

We further explored the possibility that lysosome dysfunction exists in the absence of either dMtmr6 or MTMR8. We reasoned that fusion between autophagosomes and lysosomes could be impaired, which would indicate an autolysosome formation defect and could explain increased ref(2)p/p62 and lipidated Atg8a/LC3B levels. To determine if autolysosomes form, we used the tandem GFP-mCherry-Atg8a fluorescent reporter, which is a transgene expressed under control of the Atg8a promoter (Lee et al., 2016). Dual-punctate fluorescence of both GFP and mCherry reflects autophagosomes, but because GFP is pH sensitive, mCherry signal alone reflects autolysosomes. In *Drosophila* fat body from fed animals, Atg8a reporter expression is diffuse throughout the cytoplasm in control tissue, and very few puncta form autophagosomes or autolysosomes (Fig. 4 A). By contrast, *dMtmr6*-depleted tissue contains numerous autophagosomes and autolysosomes (Fig. 4, B and C). These data indicate that the number of autolysosomes increase when *dMtmr6* function is reduced.

Reduced function of both *dMtmr6* in *Drosophila* and *MTMR8* in COS-7 cells results in large Atg8a/LC3B and ref(2)p/p62 structures. To further determine the nature of the large Atg8a-positive puncta generated by *dMtmr6* depletion, we performed transmission electron microscopy (TEM) analyses of *Drosophila* midguts 2 h APF. In control animals undergoing developmental autophagy in midgut enterocytes, the cytoplasm contains autophagosomes and autolysosomes (Fig. 4 D). By contrast, *dMtmr6*-knockdown enterocytes possess large electron-poor vesicles throughout the cytoplasm (Fig. 4 E). We classified these single-membrane structures as autolysosomes (Fig. 4, F and G), but it is possible that these structures may be amphisomes that form by fusion of autophagosomes with late endosomes. Importantly, we observe similar large autolysosome structures in COS-7 cells transfected with *MTMR8* siRNA, but not in control cells (Fig. 4, H–K).

To confirm that the large structures we observe by TEM are autolysosomes and that they occur in another mammalian cell line, we costained HeLa cells with LC3B and LAMP1 antibodies to detect coincidence of autophagic and lysosomal markers, respectively. In serum-fed HeLa cells transfected with control siRNA, we observe very few LC3B-positive spots, and LAMP1 puncta appear throughout the cytoplasm (Fig. 4 L). By contrast, *MTMR8* siRNA–transfected HeLa cells contain large puncta that feature both LC3B and LAMP1 that colocalize and cluster near the perinuclear region (Fig. 4, M–R). These data indicate that depletion of both *dMtmr6* in fly tissues and *MTMR8* in primate cells promotes the formation of large autolysosomes.

Autophagosomes deliver their cargoes to lysosomes for degradation, and impaired lysosome function can lead to autophagosome accumulation and prevent autolysosome resolution. Therefore, we evaluated lysosomes in larval fat body using LysoTracker, an acidophilic dye that labels acidic organelles, to determine if *dMtmr6* influences lysosome homeostasis. In fat body from fed larvae, *dMtmr6*-knockdown cells contain more acidic organelles than neighboring WT control cells (Fig. 5, A and B). Although *dMtmr6*-knockdown cells possess increased numbers of acidic vesicles, this may not reflect an increase in functional lysosome numbers. Therefore, we evaluated cathepsin protease activity in *dMtmr6*-knockdown cells to directly evaluate lysosomal enzyme function. We tested cathepsin B protease activity using Magic red substrate, which fluoresces upon cleavage by cathepsin B. Compared with neighboring WT cells in fat body from fed larvae, Magic red fluorescence levels increase in *dMtmr6*-knockdown cells (Fig. 5, C and D). We also measured cathepsin L protein levels from fed or starved larval fat body tissues. During starvation-induced autophagy, lysosome biogenesis increases and pre- and procathepsin L levels rise in Luciferase-RNAi and *Atg1*-RNAi control tissues (Fig. 5 E). However, in *dMtmr6*-depleted tissues from fed animals, pre- and procathepsin L protein levels are greater than in controls (Fig. 5 E), indicating that cathepsin L biogenesis increases as a result of *dMtmr6* knockdown. Together these data suggest that, although lysosomes display functional qualities in *dMtmr6*, lysosome homeostasis is altered.

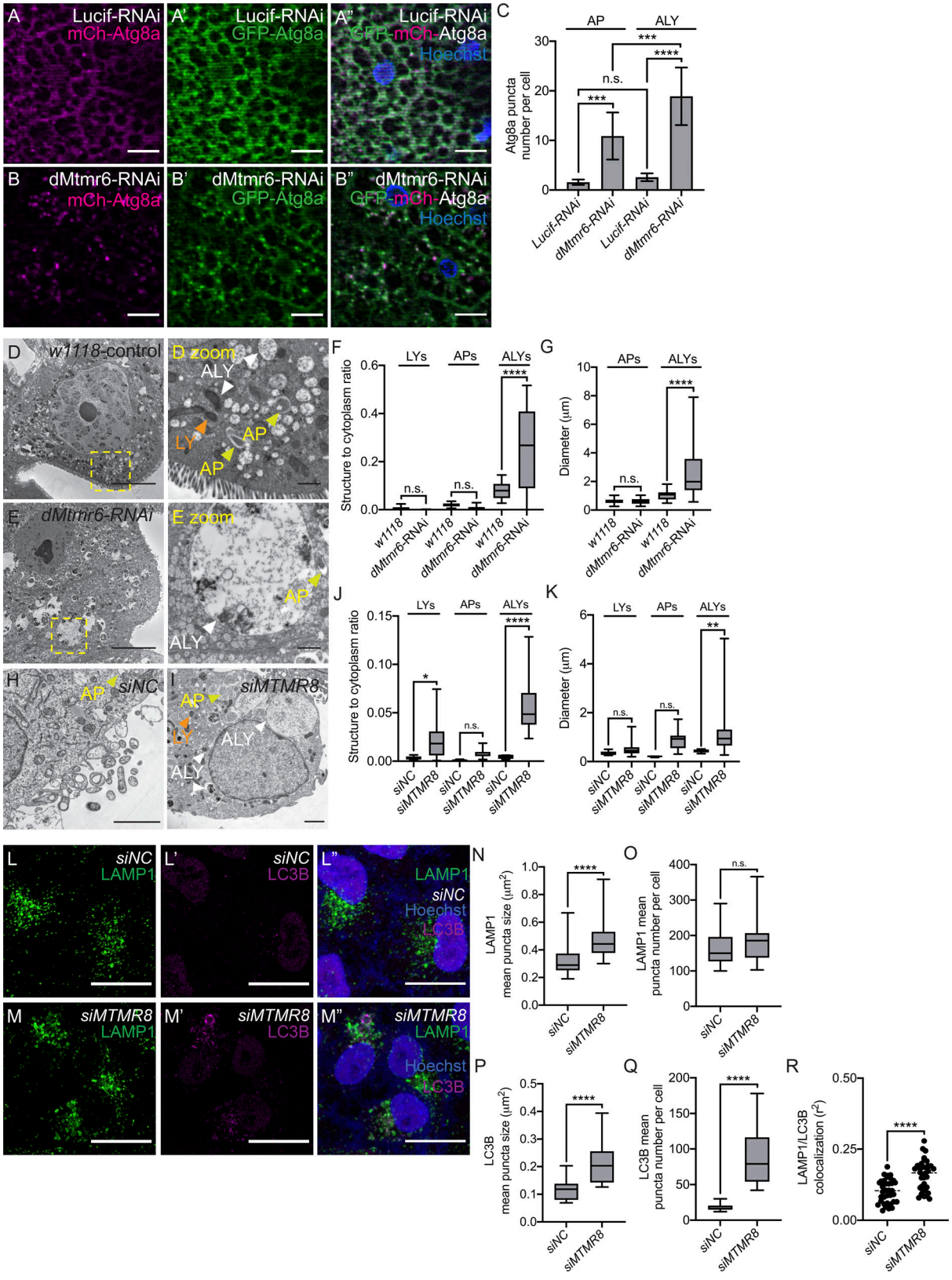

Figure 4. **dMtmr6 and MTMR8 affect autolysosome size. (A and B)** Representative images of fed L3 fat body expressing EGFP-mCherry-Atg8a and either control *Lucif*-RNAi (A) or *dMtmr6*-RNAi (B). Tissues were stained with Hoechst (blue) to detect nuclei. **(C)** Quantification of the number of Atg8a puncta expressing both GFP and mCherry (AP, autophagosomes) or mCherry only (ALY, autolysosomes) in *Lucif*-RNAi and *dMtmr6*-RNAi fat body as represented in A and B. **(D and E)** Electron micrographs of *Drosophila* larval midgut cells during developmental autophagy (2 h APF) from control *w1118* (D) or *dMtmr6* knockdown (E) tissues. Whole-cell sections on left, yellow box indicates area shown at high magnification in panels on right. Arrows indicate lysosomes (LY,

orange), autophagosomes (AP, yellow), and autolysosomes (ALY, white). **(F)** Quantification of the ratio of the indicated organelles area relative to the total area of cytoplasm. **(G)** Quantification of the diameter of indicated organelles. **(H and I)** Electron micrographs of serum-fed COS7 cells transfected with siRNA targeting scrambled *NC* control (H) or *MTMR8* (I). **(J)** Quantification of the ratio of the indicated organelles area (μm^2) relative to the total area of cytoplasm. **(K)** Quantification of the diameter of indicated organelles. **(L and M)** Representative maximum intensity projection of *z*-stack image from serum-fed HeLa cells siRNA-transfected to target *NC* control (L) or *MTMR8* (M) stained with Hoechst to detect nuclei (blue) and antibodies to detect LAMP1 (green) and LC3B (magenta), indicative of lysosomes and autophagosomes, respectively. Autolysosomes contain both LAMP1 and LC3B. **(N–R)** Quantification of the size, number, and colocalization of cellular LAMP1 and LC3B puncta as represented in L and M. Data are presented as mean ± SD, $n \geq 5$ random images taken across three samples from each genotype (C); and as mean ± minimum to maximum (F, G, J, K, and N–R), with $n \geq 10$ random images taken across samples from three biological replicates (F and G), $n = 15$ images per genotype, and one experimental replicate in (J and K), or $n = 10$ images per genotype and three experimental replicates (O–S). Asterisks denote statistical significance (*, $P < 0.05$; **, $P < 0.01$; ***, $P < 0.001$; ****, $P < 0.0001$) using one-way ANOVA (C, F, G, J, and K) and unpaired, two-tailed *t* test with Welch's correlation (O–S). Scale bars represent 20 µm (A, B, L, and M), 10 µm (D and E, left panels), 1 µm (D [zoom] and E [zoom], right panels), and 2 µm (H and I).

Because lysosomal homeostasis is altered in *dMtmr6* knockdown cells, we reasoned that aspects of the endolysosomal pathway may be altered. To test whether *dMtmr6* functions in endocytosis, we monitored fluid-phase endocytosis in larval fat body via uptake of Texas red (TR)-avidin. Control cells contained TR-avidin–positive puncta throughout the cytosol, whereas *dMtmr6*-knockdown cells (GFP positive) possessed little to no endocytic tracer (Fig. 6, A and B), suggesting that *dMtmr6* depletion impairs early endocytic uptake. However, we observed no change in localization of the endosomal marker Rab7 (Fig. S2, G–I). Thus, *dMtmr6* knockdown alters endocytosis in a manner that does not appear to impact Rab7 localization.

Intracellular localization of FYVE domain–containing proteins represents PI(3)P-enriched sites (Gillooly et al., 2000). However, *Drosophila* PI(3)P reporters remain limited to endosomal compartments, and we lack tools that are specific to autophagic PI(3)P. Nonetheless, we investigated how *dMtmr6* depletion effects the widely used GFP-2xFYVE endosomal PI(3)P reporter, which utilizes two copies of the FYVE domain from the early endosomal protein Hrs fused to EGFP (Wucherpfennig et al., 2003). When we misexpressed GFP-2xFYVE and depleted *dMtmr6* in fat body of fed larvae, we detected increased GFP-2xFYVE levels in cellular regions that are both perinuclear and away from the nucleus (aponuclear) when compared with *Lucif-RNAi* controls (Fig. S3, A–F). Interestingly, fat body from fed *dMtmr6*-knockdown animals contained perinuclear GFP-2xFYVE distribution similar to fat body from starved control animals, even though aponuclear levels remained high in *dMtmr6-RNAi* conditions (Fig. S3, B–G). Starvation further increased perinuclear and decreased aponuclear GFP-2xFYVE localization in *dMtmr6*-depleted cells (Fig. S3, C–H). Despite alterations in GFP-2xFYVE localization, we saw reduced colocalization between GFP-2xFYVE and Atg8a in *dMtmr6*-knockdown cells compared with controls in both fed and starved conditions (Fig. S3, I–M). Together, these data indicate that *dMtmr6* depletion impacts localization of PI(3)P-containing vesicles, but these vesicles remain distinct from large Atg8a-bearing structures.

Phagocytosis requires both Vps34-mediated PI(3)P generation and lysosomal degradation of extracellular cargoes (Jeschke and Haas, 2016). Given the role of dMtmr6 in autophagy and endocytosis, we hypothesized that dMtmr6 might also influence phagocytosis. To investigate this, we tested the ability of *Drosophila dMtmr6*-knockdown embryonic macrophages to engulf apoptotic corpses, which are generated throughout the embryo as part of normal development. Corpse phagocytosis primes macrophages for subsequent immune responses such as recruitment to wounds and bacterial uptake (Weavers et al., 2016). Importantly, *dMtmr6* knockdown in embryonic macrophages compromises phagocytosis, as indicated by the decreased vacuole number compared with control macrophages (Fig. 6, C and D). These data suggest a role for dMtmr6 in phagocytosis.

dMtmr6-mutant cells are autophagy prone

We next investigated the relationship between *dMtmr6* and upstream regulators of autophagy. Cell growth and the factors that regulate this process, such as the ribosomal protein kinase p70 S6 and the serine/threonine kinase Akt (protein kinase B), often have a reciprocal relationship with autophagy. Since our data indicate that cells with decreased *dMtmr6* function are prone to autophagy, we tested if growth signaling is altered in these cells. Indeed, fat body from feeding larvae possess reduced levels of both phosphorylated p70 S6 Kinase and phosphorylated AKT in *dMtmr6*-depleted tissue compared with controls (Fig. 7 A). These data suggest that fat body exists in an autophagy-prone state in the absence of *dMtmr6*.

We queried the relationship between *dMtmr6* and the Atg1 and Vps34 kinases that are conserved regulators of autophagy (Galluzzi et al., 2017). As expected, *Atg1* knockdown alone resulted in ref(2)p accumulation (Fig. 7 B) and inhibited Atg8a puncta formation (Fig. 7, F and D). Surprisingly, fat body with double knockdown of *Atg1* and d*Mtmr6* possessed Atg8a lipidation, ref(2)p accumulation (Fig. 7 B), and increased numbers of Atg8a-positive structures (Fig. 7, C and D), but these Atg8a puncta were significantly smaller (Fig. 7, C–E). These data suggest that dMtmr6 functions in at least a partially Atg1-independent manner.

During autophagy, Vps34 kinase activity contributes to PI(3)P production on autophagic membranes, and *Vps34* mutant cells fail to form GFP-Atg8a puncta (Juhász et al., 2008). Because dMtmr6 is a putative PI(3)P phosphatase, we reasoned that dMtmr6 could influence the pool of PI(3)P that is supplied by Vps34. We used the FLP/FRT system to generate *Vps34*-null mutant cell clones in fat body expressing *dMtmr6*-RNAi (*Lsp2-GAL4 > UAS-dMtmr6-RNAi*) and evaluated Atg8a puncta formation in starved animals. *Vps34* null mutant cells that express *dMtmr6-RNAi* possess fewer Atg8a puncta than cells expressing *dMtmr6*-RNAi alone (Fig. S4, A and B). In addition, we observed

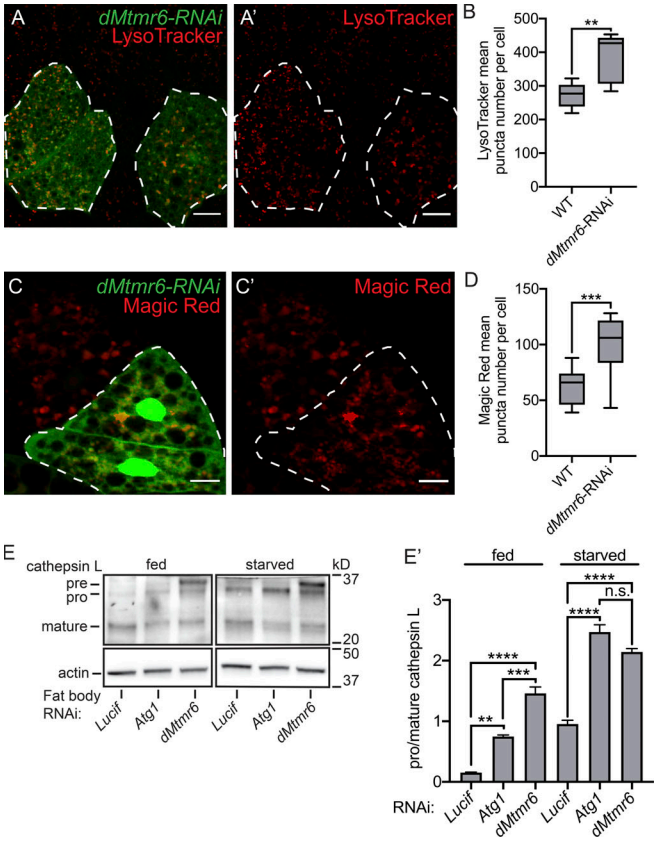

Figure 5. **dMtmr6 and MTMR8 maintain endolysosomal homeostasis.** **(A)** Representative image of fat body from fed L3 *Drosophila* larvae with control (GFP-negative) and clonal d*Mtmr6*-knockdown cells (white dotted outline, green) stained with LysoTracker red to detect acidic vesicles and LysoTracker red only depicted in A′. **(B)** Quantification of LysoTracker red puncta number in WT versus d*Mtmr6*-knockdown cells as represented in A. **(C)** Representative image of fat body from fed L3 *Drosophila* larvae with control (GFP-negative) and clonal d*Mtmr6*-knockdown cells (white dotted outline, green) stained with Magic red to detect cathepsin B protease activity and Magic red only depicted in B′. **(D)** Quantification of Magic red puncta number in WT versus d*Mtmr6*-knockdown cells as represented in C. **(E)** Representative Western blot of fat body cathepsin L protein levels from fed and starved fat body–specific knockdown larvae (L3) of the indicated genotype (*CG-Gal4 > UAS-RNAi*). **(E′)** Quantification of the ratio of procathepsin L to mature cathepsin L. Data are presented as mean ± minimum to maximum, *n* = 10 (C and D); and mean ± SEM, *n* = 6 animals for each genotype of three experimental replicates (E). Asterisks denote statistical significance (**, P < 0.01; ***, P < 0.001; ****, P < 0.0001), paired two-tailed *t* test (B and D) and one-way ANOVA (E). Scale bars, 20 µm (A and C). n.s., not significant.

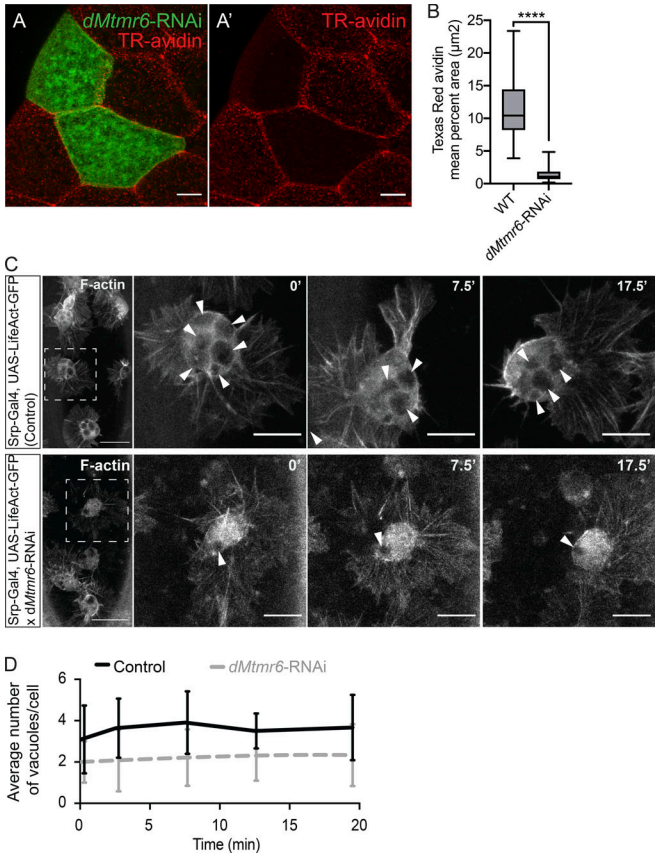

Figure 6. ***dMtmr6* depletion impairs endocytosis and phagocytosis.** **(A)** Representative image of TR-avidin (red)-treated fat body from fed L3 *Drosophila* larvae with WT control (GFP-negative) and clonal *dMtmr6*-knockdown (green) cells and TR-avidin only depicted in A′. Tissues were fixed following ex vivo incubation with TR-avidin as described in Materials and methods. **(B)** Quantification of percent area (µm^2) of TR-avidin in WT versus *dMtmr6*-knockdown cells as represented in A. **(C)** Control *Drosophila* macrophage expressing GFP-labeled F-actin (top panels), which contain phagocytic vacuoles (arrowheads) during developmental apoptotic corpse clearance in embryos, compared with *dMtmr6*-knockdown *Drosophila* macrophages expressing GFP-labeled actin (bottom panels). **(D)** Quantification of the number of phagocytic vacuoles in macrophages over time from control versus *dMtmr6*-knockdown cells. Data are presented as mean ± minimum to maximum (*n* = 10 paired WT and *dMtmr6*-knockdown cells taken across random images from three experimental replicates; B) and mean ± SD (*n* ≥ 11; C). Asterisks denote statistical significance (****, P < 0.0001), using paired two-tailed *t* test. Scale bars represent 20 µm (A), 20 µm (C, first panel from left), and 10 µm (C, second panel from left).

similar results when we tested if the loss of *Atg9* could suppress Atg8a puncta formation in *dMtmr6*-knockdown tissue (Fig. S4, C and D). Taken together, these data suggest that dMtmr6 negatively regulates Atg8a membrane association and that dMtmr6 function is at least partially independent of either *Vps34*, *Atg9*, or *Atg1* function.

Autolysosomal homeostasis requires the MTMR8 PH-GRAM domain and catalytic cysteine residue

Despite documentation that MTMR8 hydrolyzes PI(3)P and PI(3,5)P_2 in vitro (Zou et al., 2012a, 2012b), we lack evidence that the MTMR8 catalytic domain mediates autophagy. In fact, MTMR8 could influence autophagy by various membrane interactions, including PI(3)P or PI(3,5)P_2 hydrolysis (CX_5R motif) and membrane localization (PH-GRAM domain), which are required for other MTMR family members (Amoasii et al., 2012). To test these possibilities, we modified MTMR8 in HeLa cells using CRISPR-Cas9 to generate a cysteine to serine mutation (MTMR8-C338S), which is the amino acid change seen in the catalytically dead MTMR family members, and a PH-GRAM domain truncation (MTMR8ΔPH; Fig. 8 A; Lorenzo et al., 2006). Similar to the LAMP1 and LC3B puncta alterations in *MTMR8*-knockdown cells (Fig. 4, M–S), LAMP1 and LC3B vesicles were larger in serum-fed MTMR8-C338S cells than in

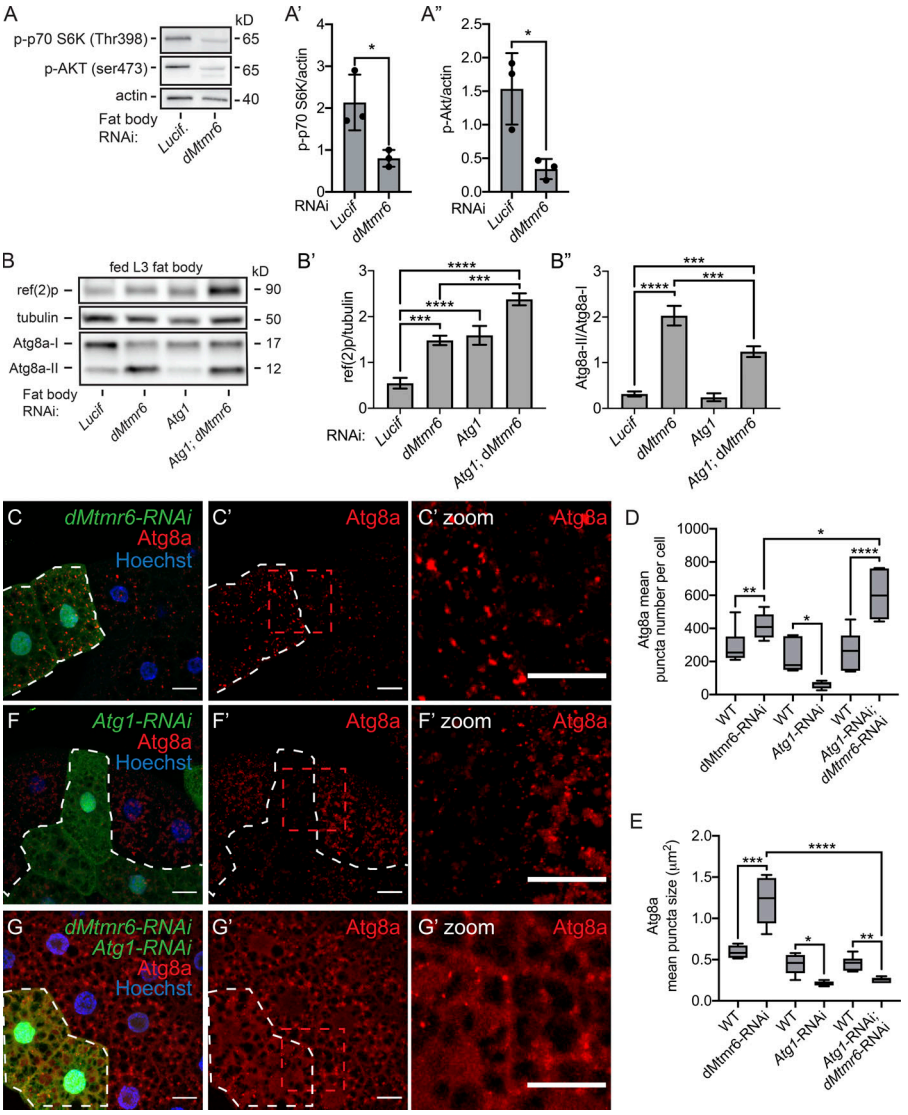

Figure 7. **dMtmr6 regulates autophagic flux independently of Atg1. (A)** Representative Western blot from fat body of indicated genotypes to measure levels of phosphorylated p70-S6K (A′) and phosphorylated AKT (Av) proteins relative to actin. **(B)** Representative Western blot using fed L3 fat body from fat body–specific knockdown of the indicated genotypes (*CG-Gal4 > UAS-RNAi*) to measure the ratio of lipidated to cytosolic Atg8a (B′) and ref(2)p to actin (B″) protein levels. **(C, F, and G)** Representative images of starved L3 fat body with control (GFP-negative) and knockdown cells of indicated genotypes (white dashed outline, green cells) stained with an antibody to detect Atg8a and Hoechst to detect nuclei (blue). Atg8a only is depicted in C′, F′, and G′, and red boxes indicate areas shown in zoom panels at right. **(D and E)** Quantification of cellular Atg8a puncta number (D) and average size (E) as represented in C, F, and G. Data are presented as mean ± SD, $n = 6$, three experimental replicates (A and B) or mean ± minimum to maximum ($n \geq 9$; D and E). Asterisks denote statistical significance (*, $P < 0.05$; **, $P < 0.01$; ***, $P < 0.001$; ****, $P < 0.0001$), using unpaired two-tailed *t* test (A) and one-way ANOVA (B, D, and E). Scale bars, 20 µm.

MTMR8-WT cells (Fig. 8, B–E). Furthermore, fewer LAMP1 puncta, more LC3B puncta, and increased LAMP1/LC3B co-localization exist in MTMR8-C338S cells compared with MTMR8-WT control cells (Fig. 8, F–H). Although not significant, MTMR8-C338S influences autophagic flux in serum-fed conditions compared with control cells (Fig. S5). Furthermore, LysoTracker staining appears brighter in MTMR8-C338S cells compared with MTMR8-WT cells, but puncta number and size remains unchanged (Fig. S5, B–E). These data suggest that MTMR8 catalytic activity influences autophagic flux.

We next investigated the requirement of the MTMR8PH-GRAM domain for autophagy. In striking comparison to both MTMR8-WT and MTMR8C338S cells, MTMR8ΔPH cells contain enlarged LAMP1 and LC3 puncta, reduced LAMP1 and increased LC3B puncta numbers, and significant colocalization between these two autophagic markers (Fig. 8, B–I). Moreover, MTMR8ΔPH cells have more LysoTracker puncta than both MTMR8-WT and MTMR8-C338S cells, and LysoTracker staining significantly overlaps with LAMP1 (Fig. S5, D–G). Thus, MTMR8 catalytic function influences autophagy, but MTMR8 membrane localization via the PH-GRAM domain appears to play a more critical role in autolysosome homeostasis.

Previous data indicate that MTMR8 favors PI(3)P, but can hydrolyze both PI(3)P and PI(3,5)P2 (Zou et al., 2012b). To investigate a role for MTMR8 in PI(3)P-regulation at autophagic membranes, we evaluated localization of WIPI2, a protein that binds early autophagic structures at PI(3)P-enriched sites (Dooley et al., 2014). We found a significant increase in WIPI2 puncta numbers in both MTMR8C338S and MTMR8ΔPH cells compared with MTMR8-WT control HeLa cells (Fig. 8, J–O), which suggests that MTMR8 regulates PI(3)P levels at autophagic membranes. Furthermore, MTMR8C338S cells contain significantly more WIPI2 puncta than MTMR8ΔPH cells (Fig. 8, K–M and O), indicating that the catalytic cysteine residue is important for decreasing PI(3)P levels, while the PH domain is likely important for MTMR8 recruitment to PI(3)P-bearing membranes. Moreover, WIPI2 and LC3B colocalize more in MTMR8C338S cells and less in MTMR8ΔPH cells (Fig. 8, K, N, and O). We expected that impaired PI(3)P hydrolysis by MTMR8C338S could lead to increased WIPI2 recruitment, more

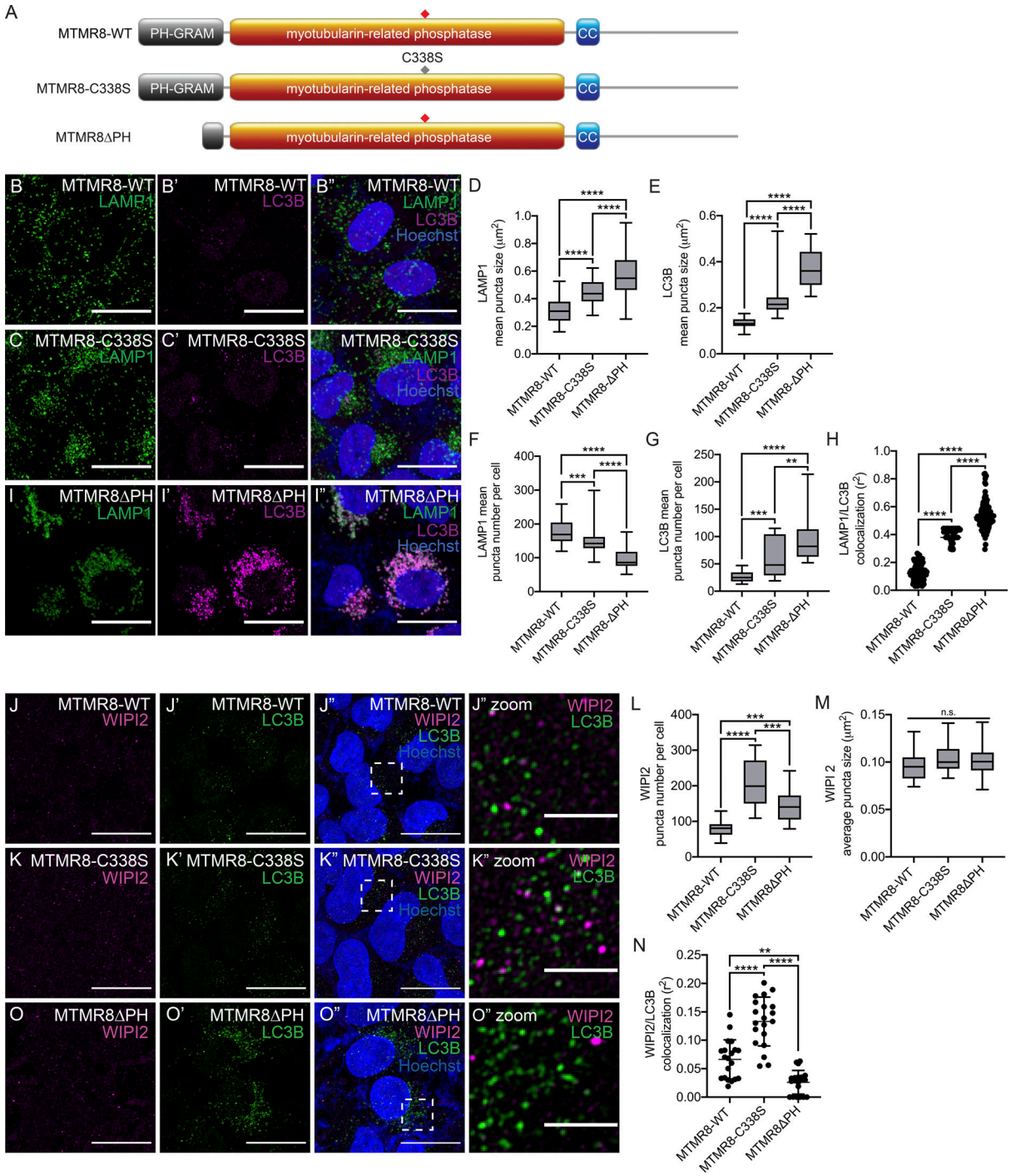

Figure 8. **Autolysosome homeostasis requires the MTMR8 PH-GRAM domain and catalytic cysteine residue. (A)** Schematic of MTMR8 mutants used in (B, C, I, J, K, and O). An intact PH-GRAM domain and catalytic cysteine residue exist in WT MTMR8, MTMR8-C338S features a serine in place of the catalytic cysteine, and the PH-GRAM domain is truncated in MTMR8ΔPH. **(B, C, and I)** Representative maximum intensity projection of z-stack image from HeLa cells with the indicated genotypes stained with Hoechst to detect nuclei (blue) and antibodies to detect LAMP1 (green) and LC3B (magenta), indicative of lysosomes and autophagosomes, respectively. Autolysosomes contain both LAMP1 and LC3B. **(D–H)** Quantification of the size, number, and colocalization of both LAMP1 and LC3B puncta per cell as represented in B, C, and I. **(J, K, and O)** Representative maximum intensity projection of z-stack image from HeLa cells with the indicated genotypes stained with Hoechst to detect nuclei (blue) and antibodies to detect WIPI2 (magenta; J, K, and O) and LC3B (green; J′, K′, and O′), with merged channels shown in J″, K″, and O″ and dashed white boxes indicating the areas shown in zoom panels at the right. **(L–N)** Quantification of the number and size of WIPI2 puncta and colocalization between WIPI2 and LC3B as represented in J, K, and O. Data are presented as mean ± minimum to maximum ($n \geq 5$ cells per 10 random images from three experimental replicates (D–H and L–N). Asterisks denote statistical significance (**, P < 0.01; ***, P < 0.001; ****, P < 0.0001), using one-way ANOVA. Scale bars, 20 μm.

LC3B conjugation, and increased WIPI2/LC3B colocalization. However, it is surprising that WIPI2/LC3B colocalization decreases in MTMR8ΔPH cells compared with MTMR8-WT control cells when WIPI2 puncta numbers increase, suggesting a possible role for the MTMR8 PH domain in WIPI2/LC3B localization.

Previous work indicates that MTMR8 localizes to the perinuclear region (Lorenzo et al., 2006). We surmised that MTMR8 might localize to a perinuclear lysosomal pool to facilitate autolysosome resolution. We initially used CRISPR-Cas9 to tag the MTMR8 C-terminus with 3xFLAG, but we were unable to detect FLAG by either immunofluorescence or immunoblotting. Therefore, we overexpressed MTMR8. Unlike Lorenzo et al., we saw peripheral localization, and MTMR8 failed to overlap with perinuclear-localized LC3B puncta (Fig. S5 H). Consistent with previous work (Zou et al., 2012b) and our evidence that MTMR8 influences autophagic flux (Fig. 3), p62 protein levels decreased and lipidated LC3B levels increased in cells overexpressing MTMR8 (Fig. S5 I). While MTMR8 mutant and overexpression differentially influence p62 levels, LC3B-II levels increase under both conditions. These data suggest that MTMR8 overexpression activates autophagy and promotes degradation, while MTMR8 inactivation impairs degradation, which activates autophagy through what is likely a TFEB-mediated feedback loop. Taken together, these data suggest that MTMR8 influences autophagic flux by promoting lysosome-mediated degradation.

Discussion

We identified *Drosophila CG3530/Mtmr6* as a positive regulator of autolysosome homeostasis and show that *MTMR8* has a similar function in both human and monkey cells. *dMtmr6* maintains autophagic flux in multiple fly tissues under different conditions, including stress- and developmentally induced autophagy. We demonstrated that dMtmr6 and MTMR8 play a critical role in regulating the amount and size of cellular Atg8a/LC3B-positive vesicles. Furthermore, these structures correlated with lysosome markers and demarcated the existence of autolysosomes. Depletion of *dMtmr6* in fly tissues or *MTMR8* in mammalian cells influences endolysosomal homeostasis and promotes autolysosome accumulation.

MTMRs dictate intracellular membrane identity and modulate membrane trafficking events, including autophagy, through PI(3)P and PI(3,5)P_2 degradation. However, differential expression of MTMRs implies that they may have cell- and tissue-specific functions (Raess et al., 2017). According to bioinformatics studies from public data at the Genotype-Tissue Expression database, the roles and requirements for the different MTMRs are thought to differ according to tissue and cell type. For example, *MTMR8* is expressed at higher levels in reproductive tissues than in brain tissues, which instead, express *MTMR7*. Meanwhile, *MTMR6* is most highly expressed in the adrenal gland and testis. We tested HEK293T cells (kidney) in our analyses (not shown) and found that *MTMR8* knockdown had a less significant effect on autophagic structures than in HeLa cells (cervical). These data are consistent with the data of Raess et al. (2017), which show lower *MTMR8* expression in kidney and higher *MTMR8* expression in cervical tissues. Like *MTMR8*, publicly available RNA sequencing of *Drosophila* tissues indicates that *dMtmr6* is highly expressed in reproductive tissues, and both *MTMR8* and *dMtmr6* are moderately expressed in tissues of the digestive tract (Thurmond et al., 2019). Unlike *MTMR8*, however, *dMtmr6* is highly expressed in head of adult flies, hinting at a role for dMtmr6 in the brain and potentially the central nervous system. Interestingly, *dMtmr6* muscle-specific knockdown impairs *Drosophila* flight (Schnorrer et al., 2010).

Tissue and cell specificity at least partially account for the diverse regulatory functions of the MTMR6 subfamily members and their binding partner, MTMR9. Human MTMR6 facilitates PI(3)P turnover during micropinocytosis (Maekawa et al., 2014), negatively regulates the Ca^{2+}-activated K^+ channel KCa3.1 in CD4 T cells (Srivastava et al., 2005, 2009), and apoptosis in HeLa cells (Zou et al., 2009a, 2012a). Similar to *dMtmr6*, which regulates AKT signaling in *Drosophila* fat body (Fig. 7 A), both MTMR7 and MTMR9 regulate CD4 T cell AKT signaling and differentiation (Guo et al., 2013), and MTMR7 regulates AKT signaling in C2C12 myoblasts. MTMR7 protein levels inversely correlate with tumor grade in colorectal cancer (CRC), and in CRC cell lines, MTMR7 inhibits proliferation and insulin-mediated AKT-ERK1/2 signaling (Weidner et al., 2016). In zebrafish embryos, MTMR8 regulates actin filament modeling (Mei et al., 2009) and both muscle (Mei et al., 2009) and vascular development (Mei et al., 2010). It is important to note that the mouse genome lacks MTMR8 and contains only MTMR6 and MTMR7. In human cells, the MTMR8–MTMR9 complex reduces PI(3)P levels and inhibits autophagy (Zou et al., 2012b). MTMR9 mutations are associated with obesity (Yanagiya et al., 2007), metabolic syndrome (Hotta et al., 2011), and multiple prediabetes-associated symptoms (Tang et al., 2014). While a specific link to MTMR8 in disease remains to be determined, alterations in the MTMR8 locus have been implicated in glioblastoma multiforme (Waugh, 2016) and intellectual disability (Holman et al., 2013). Furthermore, a rare type of X-linked spastic paraplegia (SPG16; OMIM accession no. 300266) is mapped to an uncharacterized locus at Xq11.2, which is where MTMR8 resides. Future studies could benefit from mining genome- and exome-sequencing databases for the influence of this MTMR family on disease.

An additional difference exists between *MTMR8* and *dMtmr6*. *MTMR8* encodes one human isoform while *dMtmr6* encodes three (Fig. 2 A). We have not experimentally tested the significance of *dMtmr6* splice isoforms. However, publicly available data of fly gene expression during development indicate that there is ubiquitous expression of *dMtmr6* B and C isoforms throughout development (Thurmond et al., 2019). The *dMtmr6* A isoform is expressed at low levels during early embryonic development, ceases during late embryonic development, and increases progressively throughout the L3 stage. In adult flies, isoform A expression is lower in females than in males. Potentially relevant to our findings, wandering third-instar fat body expresses both B and C, but not A. However, upon pupa formation, when numerous tissue types undergo developmental autophagy, all three isoforms are expressed. Thus, *dMtmr6*

isoform A could play a specific role in developmental autophagy, while isoforms B and C function more generally. Our data indicate that *dMtmr6* is required for survival (Fig. 2 B), yet some trans-heterozygous animals that are $dMtmr6^{KG01267}/Df(2R)$ survive to adults. The $dMtmr6^{KG01267}$ allele retains isoform A, which indicates that, in the absence of isoforms B and C, isoform A could function in a compensatory way to support survival. Future experiments should explore the possibility of isoform-specific *dMtmr6* functions in development and cellular trafficking.

Despite evidence of autophagy initiation, *dMtmr6* and MTMR8 depletion elicits ref(2)p/p62 accumulation, indicative of impaired autophagic cargo degradation (Fig. 2 C; and Fig. 3, A–D and G–M). However, autophagosome–lysosome fusion remains intact based on GFP signal reduction in *dMtmr6* fat body expressing the tandem-fluorescent Atg8a reporter (Fig. 4, A–C). This reporter recapitulated the aberrant large autophagic puncta we saw with mCherry-Atg8a alone in *dMtmr6*-depleted fat body from fed animals and supplied evidence that upon fusion, lysosomal pH remains low enough to quench the GFP signal from autophagic structures. Furthermore, *dMtmr6*-depleted cells possess elevated levels of LysoTracker and cathepsin B protease activity compared with adjacent WT cells (Fig. 5, A–D). These data imply that in *dMtmr6*-deficient cells, lysosomes harbor some functional characteristics that are required for degradation. Similarly, *MTMR8*-deficient and mutant cells possess numerous and large vesicles that are positive for LC3B, LAMP1, and LysoTracker, indicative of acidified autolysosomes (Fig. 4, L–R; Fig. 8, B–I; and Fig. S4, B–G). Thus, in *dMtmr6*- and *MTMR8*-depleted cells, autophagosomes form and fuse with lysosomes, which suggests that they promote postfusion endolysosomal homeostasis. Despite aberrant localization, the endosomal marker GFP-FYVE failed to colocalize with large Atg8a-positve vesicles in *dMtmr6*-knockdown tissue (Fig. S3). This suggests that although autophagic vesicles lack endosomal markers in *dMtmr6*-depleted cells, inactivation of *dMtmr6* may interfere with endocytic trafficking via a direct or indirect role at endocytic vesicles or degradative lysosomes, respectively. Taken together, our data indicate that dMtmr6/MTMR8 may regulate autophagy at the autolysosome. Future studies should investigate if dMtmr6/MTMR8 mediates autolysosome reformation.

We also evaluated *Drosophila* cathepsin L protein levels (Fig. 5 E). Lysosomal cathepsins are synthesized as inactive preproenzymes that undergo subsequent maturation steps (Stoka et al., 2016). Following preprocathepsin synthesis in the ER, the N-terminal signal peptide is cleaved and glycosylated to generate procathepsin. Glycosylation ensures that cathepsins remain inactive until low pH triggers propeptide unfolding and either successive autocleavage or cleavage by other active cathepsins. We showed that cathepsin L undergoes maturation in *dMtmr6*-depleted *Drosophila* fat body from fed and starved animals, but the balance between preprocathepsin, procathepsin, and mature cathepsin L differs compared with WT fat body under the same conditions (Fig. 5 E). Indeed, high levels of prepro- and procathepsin L exist in *dMtmr6*-knockdown tissue. For this, one possible explanation is that *dMtmr6* deficiency influences cathepsin L processing. However, we can detect mature cathepsin L, and an alternative possibility is that *dMtmr6* depletion prompts lysosome biogenesis. This idea is further supported by our evidence of augmented gene expression of known targets of Mitf (TFEB) in *dMtmr6*-depleted tissues (Fig. S2 F), denoting activation of autophagy and lysosome biogenesis (Sardiello et al., 2009). We note that *dMtmr6*-knockdown elevates *ref(2)p* transcript levels, which could also compound ref(2)p protein levels. It appears that *MTMR8*-depleted cells undergo a similar response because TFEB localized to the nucleus of HeLa cells under both serum-fed and serum-starved conditions.

Phosphorylated p70 S6K and Akt levels are reduced in *Drosophila dMtmr6*-knockdown fat body from fed animals compared with control animals (Fig. 7 A), which likely explains the influence of bMtmr6/MTMR8 on Mitf/TFEB. Indeed, both phospho-p70 S6K and phospho-Akt are indicators of mTORC1 activity and phosphorylation is indicative of ample nutrients and growth factors (Liu and Sabatini, 2020). When active, mTORC1 localizes to lysosomes and inhibits TFEB nuclear localization (Settembre et al., 2012), and Akt represses TFEB nuclear localization independent of mTORC1 (Palmieri et al., 2017). Conversely, starvation and lysosome stress prompts mTORC1 dissociation from lysosomes, TFEB nuclear translocation, and autophagy induction (Settembre et al., 2012). During prolonged starvation, cells require mTORC1 reactivation to replenish the lysosome pool (Yu et al., 2010). Furthermore, active mTORC1 is required for lysosomal tubulations, which is a critical step in autolysosome reformation (Yu et al., 2010). Once reactivated, mTORC1 functions upstream of PIK3C3 produce a small pool of autolysosomal PI(3)P, and loss of PIK3C3 activity, despite active mTORC1, prevents tubule scission. Our genetic epistasis analyses indicated that *dMtmr6* functions at least in a partially class III PI3K Vps34–independent manner (Fig. S3 A and B). As mentioned above, our data suggest that *dMtmr6* functions at the autolysosome to facilitate degradation. In *Drosophila* blood cells, the class II PI3K, Pi3K68D coregulates endolysosomal size and cortical dynamics with mtm, an MTMR family member, via a pool of PI(3)P (Velichkova et al., 2010). However, endolysosomal size in blood cells is also *Atg1* and *Vps34*-dependent, unlike *dMtmr6*. The results of our phosphatase screen indicate that mtm does not play a role in fat body or developmental midgut autophagy (Table S1). Moreover, we do not think that *dMtmr6* plays a role in cortical remodeling of blood cells. We were able to observe actin filaments (as seen by LifeAct localized accumulation) at extending protrusions in both control and *dMtmr6*-depleted blood cells (Fig. 6 C), which strongly suggests that *dMtmr6* does not play a direct role in actin filament turnover.

We showed that *dMtmr6*-depleted macrophages contained fewer phagocytic vacuoles than control blood cells (Fig. 6 C). Phagocytosis requires Vps34 to produce PI(3)P and, like autophagy, terminates as lysosomal hydrolases degrade cargoes (Jeschke and Haas, 2016). During *Drosophila* embryonic development, apoptotic corpses are removed by macrophages, a process that primes these blood cells for ensuing immune responses later in life (Weavers et al., 2016). Our findings imply that *dMtmr6* supports macrophage corpse uptake. Similarly, we saw impaired uptake of TR-avidin by fluid-phase endocytosis in *dMtmr6*-depleted fat body cells (Fig. 6 A). In the nematode

Caenorhabditis elegans, MTM-1, MTM-6, and MTM-9 facilitate fluid-phase endocytosis in coelomocytes (Dang et al., 2004; Xue et al., 2003), and MTM-1 negatively regulates apoptotic corpse engulfment (Neukomm et al., 2011; Zou et al., 2009b). Thus, MTMRs have an evolutionarily conserved role in these diverse but related trafficking processes.

Here, we demonstrate that dMtmr6 and MTMR8 positively regulate late-stage autophagy and play a critical role in regulating autophagic flux. Our analyses revealed critical requirements for dMtmr6 and MTMR8 in preventing expansion of the Atg8a/LC3B compartment, leading to autolysosome accumulation, and impairing autophagic flux in multiple cell and tissue types. Defects in autophagic flux underlie lysosomal storage disorders and neurodegenerative diseases, including Parkinson's and Huntington's. Thus, it remains important to identify novel drug targets to modulate autophagy levels. Future studies of MTMR6 family members will reveal if they are useful targets to mitigate human diseases.

Materials and methods

Fly stocks

Drosophila were raised on standard cornmeal-molasses-agar medium. We performed fly crosses and experiments at 25°C unless noted otherwise. We used *UAS-Luciferase* as the WT control for RNAi experiments. We used CRISPR-Cas9 to delete the *dMtmr6* open reading frame (Well Genetics). To generate RNAi-expressing cell clones, we crossed *yw hsFlp*; pmCherry-*Atg8a*; *Act*>CD2> Gal4, *UAS-GFP* (nls) virgin females to *UAS-RNAi* males. To generate tissue-specific knockdown, we crossed *Npl*-Gal4 virgins for intestinal knockdown or *CG*-Gal4 virgins for fat body knockdown to *UAS-RNAi* males. For *dMtmr6* mutant cell clones we crossed *yw hsFlp*; *FRT42D, ubi-GFP* virgin females to *FRT42D, dMtmr6Δ* males. For tandem-fluorescent Atg8a analyses, we used the EGFP-mCherry-Atg8a that is expressed ubiquitously under the control of the Atg8a promoter (Lee et al., 2016). For *Vps34* and *Atg9* mutant clones, we crossed *yw hsFlp*; *FRT42D, ubi-RFP*; *Lsp2*-Gal4 to either *yw hsFlp; FRT42D, Vps34$^{\Delta m22}$/cyo; dMtmr6-RNAi^{BL38340}* or *yw hsFLP; FRT42D, Atg9^{d51}/cyo; dMtmr6-RNAi^{BL38340}*. The following fly stocks used were from the Bloomington Drosophila Stock Center (BDSC): *UAS-CG3530^{HMS01807}*, *UAS-Luciferase^{35788}*, *UAS-GFP-myc-2xFYVE^{42712}*, and *CG-Gal4^{7011}*. The sequences for BDSC knockdown strains are available via the *Drosophila* RNAi Screening Center and Transgenic RNAi Project (DRSC/TRiP) at https://fgr.hms.harvard.edu. We used RNAi lines from the Vienna *Drosophila* RNAi Center (VDRC; UAS-*Atg1^{GD16133}*, UAS-*CG3530^{GD26216}*). The sequences for VDRC knockdown strains are available at http://stockcenter.vdrc.at/control/main. We thank the following researchers for mutant flies: Gabor Juhász, Eotvos Lorand University, Budapest, Hungary for *Vps34$^{\Delta m22}$* (Juhász et al., 2008) and Guang-Chao Chen for *Atg9^{d51}* (Wen et al., 2017).

Induction of cell clones and quantification

We induced RNAi clones in midgut or fat body cells by crossing virgin females of *y w hsFlp; pmCherry-Atg8a; Act >CD2 >GAL4* (> is FRT site), *UAS-nlsGFP/TM6B* (reference) or *y w hsFlp; +; Act >CD2 >GAL4, UAS-nlsGFP/TM6B* to indicated transgenic RNAi lines. Following 1-d egg lays, we heat-shocked embryos at 37°C for 10 min. White prepupae were placed on wet filter paper for 2 h before dissection.

Starvation of larvae

We transferred feeding L3 to 20% sucrose (starved) for 4 h or kept larvae in food (fed).

Immunolabeling and microscopy of *Drosophila* tissues

We dissected midguts or fat body in PBS (Gibco), fixed tissues in 4% formaldehyde in PBS 0.1% Triton X-100 (PBS-TX) overnight at 4°C, blocked with 1% BSA and 0.5% cold fish skin gelatin, and incubated overnight at 4°C with primary antibodies in PBS-TX. For immunolabeling, we used rabbit anti-GABARAP (1:100; Cell Signaling Technologies; 13733), chicken anti-GFP (1:500; Abcam; ab13970), and rabbit anti-ref(2)p (1:100; Abcam; ab178440). We used Hoechst dye to stain DNA and the following secondary antibodies (1:250): anti-rabbit Alexa Fluor 546 (Thermo Fisher Scientific; A-11035), anti-mouse 546 (Invitrogen; A-11003), or anti-rat Alexa Fluor 488 or 546. We mounted samples in Vectashield (Vector Labs). We imaged samples with a Zeiss LSM 700 confocal microscope equipped with a Plan-Apochromat 63×/1.40 Oil differential interference contrast (DIC) M27 objective and EC Plan-Neofluar 40×/1.30 Oil DIC M27 objective at room temperature (22°C) using Zeiss Zen Software. For LysoTracker red staining, we dissected tissues in PBS, transferred samples to LysoTracker red diluted in PBS (1:1,000) on ice for 5 min, mounted samples in 80% glycerol (in PBS), and imaged immediately at room temperature (22°C) with a Zeiss AxioImager Z1 microscope equipped with a Plan-Apochromat 20×/0.8 M27 objective and an Axiocam MR3 camera using Axiovision Imaging software. For Magic red staining, we dissected tissues in PBS, followed by a 30-min incubation in Magic red (diluted 1:10 in PBS; ImmunoChemistry; Magic red Cathepsin B Assay, 937) and a quick wash in PBS, and then imaged immediately. For mCherry-Atg8a and GFP-2xFYVE imaging, we fixed samples briefly with 4% formaldehyde in PBS-TX, mounted in Vectashield and imaged samples with a Zeiss AxioImager Z1 microscope (described above). Image processing was preformed using ImageJ (National Institutes of Health) by cropping, converting to RGB, generating maximum intensity projections, and adding scale bars. We calculated P values using a paired *t* test for adjacent cells, an unpaired *t* test for two separate genotypes under one condition, and an ordinary two-way ANOVA for comparison of multiple genotypes or conditions. Data are plotted as either min to max or the mean ± SD.

TR-avidin uptake assay

To visualize endocytosis, we dissected fat body from feeding L3, incubated it ex vivo with TR-avidin (Invitrogen; A820) diluted in Schneider's media to a concentration of 80 µg/ml for 20 min, and then chased with 0.5% BSA in cold PBS for 10 min before overnight fixation with 4% formaldehyde. We washed the tissue three times (10 min per wash) with 0.1% Tween-20 in PBS and mounted in Vectashield (Vector Labs). We imaged samples with a Zeiss LSM 700 confocal microscope with 40×/1.30 Oil DIC M27 objective at room temperature (22°C) using Zeiss Zen Software and processed images using ImageJ .

Cell culture and immunostaining

We cultured COS7 (ATCC; CRL-1651) and HeLa cells (ATCC; CCL-2) in DMEM supplemented with 10% FBS and penicillin/streptomycin at 37°C and 5% CO_2. We applied experimental conditions and collected cells at a specific time point for either immunostaining or Western blotting. For immunostaining, we fixed cells in 4% PFA for 20 min, permeabilized in 10 µg/ml digitonin (Sigma; D141) for 15 min at room temperature, and blocked with 5% goat serum for 60 min at room temperature. We incubated cells overnight at 4°C in the following primary antibodies (diluted in 5% goat serum): rabbit anti-LC3B (1:1,000; Abcam; ab48394), mouse monoclonal anti-LAMP1 (1:1,000; BD Biosciences; 555798), mouse anti-Lamp2 (0.5 µg/ml; DSHB; H4B4), rabbit anti-p62 (1:2,000; MBL; PM045), rabbit anti-TFEB (1:1,000; Cell Signaling Technologies; 4240), and mouse anti-WIPI2 (1:500; Abcam; ab105459). After three washes with PBS, we incubated cells for 1 h at room temperature with Hoechst to stain nuclei and the following fluorescently labeled secondary antibodies (1:250): anti-rabbit Alexa Fluor 546 (Thermo Fisher Scientific; A-11035), anti-mouse 546 (Invitrogen; A-11003), or anti-rat Alexa Fluor 488 or 546. We mounted specimens with Vectashield, examined with a Zeiss LSM 700 confocal microscope with 63×/1.40 Oil DIC M27 objective at room temperature (22°C) using Zeiss Zen Software, and processed images using ImageJ by cropping, converting to RGB, generating maximum intensity projections, and adding scale bars. For serum starvation, we incubated cells in EBSS (Gibco). For Bafilomycin treatment, we incubated cells for 12 h in Bafilomycin A1 (20 µM; Sigma-Aldrich; B1793).

Transfection, RNAi, and MTMR8 overexpression

For knockdown experiments, we transfected cells with either control or siRNA oligos using Invitrogen Lipofectamine RNAiMAX (Thermo Fisher Scientific; 13778150) and cultured for 72 h before analyses. We purchased double-stranded siRNAs from GenePharma, and sequences are listed in Table S2. For MTMR8-overexpression experiments, we transfected cells with Lipofectamine 2000 Transfection Reagent (Thermo Fisher Scientific; 11668019), either as vehicle only or to deliver Myc-DDK-MTMR8 (OriGene; RC201912), and cultured for 24 h before analyses.

HeLa cell gene editing

To generate MTMR8-C338S and MTMR8ΔPH HeLa cells, we delivered a CRISPR-Cas9 ribonucleoprotein complex containing a tracrRNA–crRNA complex, which is a two-part gRNA that consists of a CRISPR RNA (crRNA) that recognizes the DNA target sequence and a transactivating crRNA (tracrRNA) that functionally base-pairs with the crRNA to form a functional gRNA, along with Cas9 enzyme, and single-stranded donor oligonucleotides (ssODNs), using electroporation with the Neon transfection system (Thermo Fisher Scientific; MPK5000; Iyer et al., 2019). We acquired tracrRNA, crRNA, Cas9, and ssODNs from Integrated DNA Technologies and identified positive single-cell clones by PCR amplification and Sanger sequencing. The gRNA and ssODN sequences are as follows: MTMR8-C338S gRNA, 5′-GGTCCCATCCATCAGAACAA-3′; MTMR8-C338S ssODN, 5′-TCTTGTCTTCACAGGCAGTGAAGGTAGAAAAGGCCAGTGTCTTAGTACATAGTTCTGATGGATGGGACCGCACAGCACAAGTCTGCTCAGTGGCTAGCAT-3′; MTMR8ΔPH gRNA–5′, 5′-GGTAGAAAACGTGAAATTGG-3′; MTMR8ΔPH gRNA–3′, 5′-GCAGTGAAATATAAACCTCA-3′; MTMR8ΔPH ssODN, 5′-GGTAACTTATTCAGTATTTTTTCCTCCAATAACAGGTAGAAAACGTGAAAAGGTTTATATTTCACTGCTCAAGCTTTCTCAGCCAGGTAGTTATGATAGT-3′.

Immunoblotting assays

We washed mammalian cells three times with PBS, added lysis buffer (50 mM Tris-HCl, pH 7.5, 150 mM NaCl, 1 mM EDTA, and 1% Triton X-100) supplemented with protease inhibitor cocktail (Thermo Fisher Scientific; 78425), and incubated for 30 min on ice. We centrifuged homogenates at 13,000 rpm for 10 min at 4°C. We subjected supernatants to SDS-PAGE electrophoresis, transferred proteins to 0.45-mm Immobilon-P polyvinylidene difluoride membranes (Millipore; IPVH00010), and detected signals using the following primary antibodies: mouse monoclonal anti-LC3 (clone 4E12, 1:1,000, MBL, M152-3), rabbit polyclonal anti-p62 (1:1,000; MBL; PM045), mouse monoclonal anti-actin (1:2,000; Proteintech; clone 7D2C10, 60008–1-Ig).

For fly tissues, we dissected fat body from larvae in PBS. We homogenized fat body in Laemmli buffer (0.1% glycerol, 2% SDS, 0.125 M Tris, pH 6.8, 0.05% β-mercaptoethanol, and 0.05% bromophenol blue) and boiled for 10 min at 100°C. Equal amounts of proteins were separated on 12% SDS polyacrylamide gels, and we transferred proteins to 0.45 mm Immobilon-P polyvinylidene difluoride membranes (Millipore; IPVH00010) according to standard procedures. We used the following primary antibodies: rabbit anti-GABARAP (1:1,000; Cell Signaling Technology; 13733), rabbit anti-Ref(2)p (1:1,000; Abcam; ab178440), mouse anti-β-tubulin (1:50; Developmental Studies Hybridoma Bank; E7), or mouse anti-β-actin (1:2,000; Proteintech; 60008–1-Ig). We used the following secondary antibodies: HRP goat anti-mouse IgG (H+L; 1:5,000; Thermo Fisher Scientific; 31430) and HRP goat anti-rabbit IgG (H+L; 1:5,000; Invitrogen, 62–6120). We performed three independent biological replicates.

Embryonic phagocytic corpse uptake assays

Embryos of the appropriate developmental stage were collected from overnight apple juice plates, dechorionated in bleach for 90 s and mounted on double-sided sticky tape on glass slides in 10S Voltalef oil (VWR). *Srp*-Gal4, UAS-*LifeAct-GFP*/(*Cyo*) embryos were used as a control. We analyzed individual hemocytes, scoring the number of vacuoles at arbitrary time points over a 20-min time lapse. Imaging was performed on a Zeiss LSM880 with Airyscan laser scanning confocal microscope. Z-stacks and time-lapse images were processed and analyzed in ImageJ, Adobe Photoshop, and Adobe Illustrator software. Graphical representations were generated in GraphPad Prism 8.

Electron microscopy

For fly tissues, we dissected intestines in PBS (Gibco) 2 h APF, fixed in a solution of 2.5% glutaraldehyde and 2% PFA in 0.1M sodium cacodylate buffer, pH 7.4 (Electron Microscopy Sciences)

for 1 h at room temperature followed by overnight fixation at 4°C in fresh fix. Following fixation, we washed the guts in 0.1M sodium cacodylate buffer, pH 7.4, post-fixed in 1% osmium tetroxide in distilled water for 1 h at room temperature and washed in distilled water. Preparations were stained en bloc in 1% aqueous uranyl acetate for 1 h at 4°C in the dark, washed in distilled water, dehydrated through a graded ethanol series, treated with propylene oxide and infiltrated in SPI-pon/Araldite for embedding. We cut ultrathin sections on a Leica UC7 microtome. Sections were stained with uranyl acetate and lead citrate and examined on a Phillips CM10 TEM. Images were taken down the length of the gut to ensure an unbiased approach. We reviewed all images and chose representative images for analyses. We measured area of organelles and cytoplasm in ImageJ, and graphical representations were generated in GraphPad Prism 8.

For COS-7 cells, we prefixed cells in 50% media (50% fix, 2.5% glutaraldehyde, and 2% PFA in 0.1 M sodium cacodylate buffer, pH 7.4; Electron Microscopy Sciences) for 5 min followed by fixation in full fix for 1 h at room temperature. Cells were then washed with 0.1 M cacodylate buffer, pH 7.4, post-fixed in 1% osmium tetroxide in distilled water for 1 h at room temperature, and washed in distilled water. Preparations were stained en bloc in 1% aqueous uranyl acetate overnight at 4°C in the dark and then washed in distilled water. The cells were then scraped and pelleted. Cell pellets were embedded in agarose, dehydrated through a graded ethanol series, treated with propylene oxide, and infiltrated in SPI-pon/Araldite for embedding. We cut ultrathin sections on a Leica UC7 microtome. Sections were stained with uranyl acetate and lead citrate and examined using a Phillips CM10 TEM.

RT-PCR

We collected RNA from fat body dissected from L3 (n = 10) using Trizol Reagent (Invitrogen) and treated with DNase. We generated cDNA from 1 µg of RNA using Superscript III Reverse transcription and oligo (dT; Invitrogen; 18080051) according to manufacturer's instruction. cDNA of indicated genes was amplified by PCR using Power SYBR Green Master Mix (Thermo Fisher Scientific; 4368577) according to manufacturer's instructions and the following specific primers: *actin5c* forward primer, 5′-GGATGG TCTTGATTCTGCTGG-3′, reverse primer, 5′-AGGTGGTTCCGC TCTTTTC-3′, PCR product size, 146 bp; *dMtmr6* forward primer, 5′-GACAGGATCTCCGCTACTCAT-3′, reverse primer, 5′-GCAGCG AAGTGTAGACATCGT-3′, PCR product size, 98 bp; *Atg1* forward primer, 5′-GTCGGGGAATATGAATACAGCTC-3′, reverse primer, 5′-GCATGTGTTTCTTGCGATGAC-3′, PCR product size, 91 bp; *Atg18* forward primer, 5′-GTGTTCGTCAACTTCAACCAGA-3′, reverse primer, 5′-TGTCCAGGGTCGAGTCCAC-3′, PCR product size, 100 bp; *Cp1* forward primer, 5′-TCAACTACACTCTGCACAAGC-3′, reverse primer, 5′-GCCAGTCCACAGATTTGGG-3′, PCR product size, 105 bp; *Mitf* forward primer, 5′-AGTATCGGAGTAGATGTG CCAC-3′, reverse primer, 5′-CGCTGAGATATTGCCTCACTTG-3′, PCR product size, 115 bp; *Ref(2)p* forward primer, 5′-AATCGAGCT GTATCTTTTCCAGG-3′, reverse primer, 5′-AACGTGCATATT GCTCTCGCA-3′, PCR product size, 148 bp. We resolved the PCR products on a 1.5% agarose gel.

Quantification and statistical analyses

All experiments were performed independently at least three times, except for TEM. For mCherry-Atg8a, ref(2)p, LysoTracker red, TR-avidin, Rab7, Magic red, or GABARAP (Atg8a) antibody/stain–labeled puncta quantification, we chose at least five random images and counted the number of puncta in GFP-positive cells versus neighboring non-GFP cells. For LC3B, p62, LAMP1, or LysoTracker antibody/stain–labeled puncta, we chose at least 10 random images per genotype. We examined an average of 10–20 cells for each group. For colocalization analyses, we used the EzColocalization plugin for ImageJ to determine the Pearson correlation coefficient per image or per region of interest (Stauffer et al., 2018). Statistical significance was analyzed by paired or unpaired two-tailed t test for single comparisons and one-way ANOVA analysis for multiple comparisons. For all analyses, data distribution was assumed to be normal but was not formally tested. A P value <0.05 was considered statistically significant. Statistics were performed using GraphPad Prism 8 software.

Online supplemental material

Fig. S1 shows the full amino acid sequence alignment of CG3530, MTMR6, MTMR7, and MTMR8. Fig. S2 shows effects of *MTMR8* and *dMtmr6* knockdown on TFEB/Mitf signaling by immunofluorescence and gene expression changes, respectively, as well as a representative image of Rab7 localization in *dMtmr6*-knockdown tissue. Fig. S3 compares the effects of control versus *dMtmr6*-knockdown on GFP-FYVE and evaluates colocalization between GFP-FYVE and Atg8a expression in fed and starved fat body. Fig. S4 shows representative images from Atg8a-stained *dMtmr6*-knockdown fat body that contains Vps34- or Atg9-null clone cells stained and quantification of Atg8a puncta number. Fig. S5 shows the effects of MTMR8 mutations and MTMR8 overexpression on autophagy protein levels and lysosome reporter localization. Table S1 shows the predicted *Drosophila* PI phosphatases, human orthologues, reagents tested, and results of the RNAi screen for regulators of midgut autophagy. Table S2 shows the siRNA sequences that were used for cell culture experiments.

Acknowledgments

We thank the Bloomington Stock Center, the VDRC, and Well Genetics for flies; the Wolfe laboratory for use of their Neon transfection system; and the Baehrecke laboratory and Yan Zhao for constructive comments.

This work was supported by National Institutes of Health grants R35GM131689 (to E.H. Baehrecke) and 5T32CA130807-10, and Wellcome Trust fellowship 107940/Z/15/Z (to W. Wood).

The authors declare no competing financial interests.

Author contributions: E.A. Allen and E.H. Baehrecke conceptualized the experiments. E.A. Allen performed and analyzed most of the experiments. C. Amato performed and analyzed macrophage phagocytosis in embryos, T.M. Fortier performed TEM, and P. Velentzas performed *Vps34* and *Atg9* epistasis analyses in fat body. E.A. Allen and E.H. Baehrecke wrote the original manuscript with contributions from the other authors,

including text associated with the data in Fig. 6, C and D, provided by C. Amato and W. Wood.

Submitted: 12 September 2019
Revised: 23 June 2020
Accepted: 3 August 2020

References

Amoasii, L., H. Hnia, and J. Laporte. 2012. Myotubularin phosphoinositide phosphatases in human diseases. *Curr. Top. Microbiol. Immunol.* 362: 209–233.

Campa, C.C., J.P. Margaria, A. Derle, M. Del Giudice, M.C. De Santis, L. Gozzelino, F. Copperi, C. Bosia, and E. Hirsch. 2018. Rab11 activity and PtdIns(3)P turnover removes recycling cargo from endosomes. *Nat. Chem. Biol.* 14:801–810. https://doi.org/10.1038/s41589-018-0086-4

Dang, H., Z. Li, E.Y. Skolnik, and H. Fares. 2004. Disease-related myotubularins function in endocytic traffic in Caenorhabditis elegans. *Mol. Biol. Cell.* 15:189–196. https://doi.org/10.1091/mbc.e03-08-0605

de Lartigue, J., H. Polson, M. Feldman, K. Shokat, S.A. Tooze, S. Urbé, and M.J. Clague. 2009. PIKfyve regulation of endosome-linked pathways. *Traffic.* 10:883–893. https://doi.org/10.1111/j.1600-0854.2009.00915.x

De Leo, M.G., L. Staiano, M. Vicinanza, A. Luciani, A. Carissimo, M. Mutarelli, A. Di Campli, E. Polishchuk, G. Di Tullio, V. Morra, et al. 2016. Autophagosome-lysosome fusion triggers a lysosomal response mediated by TLR9 and controlled by OCRL. *Nat. Cell Biol.* 18:839–850. https://doi.org/10.1038/ncb3386

Denton, D., B. Shravage, R. Simin, K. Mills, D.L. Berry, E.H. Baehrecke, and S. Kumar. 2009. Autophagy, not apoptosis, is essential for midgut cell death in Drosophila. *Curr. Biol.* 19:1741–1746. https://doi.org/10.1016/j.cub.2009.08.042

Dooley, H.C., M. Razi, H.E.J. Polson, S.E. Girardin, M.I. Wilson, and S.A. Tooze. 2014. WIPI2 links LC3 conjugation with PI3P, autophagosome formation, and pathogen clearance by recruiting Atg12-5-16L1. *Mol. Cell.* 55:238–252. https://doi.org/10.1016/j.molcel.2014.05.021

Dowling, J.J., S.A. Moore, H. Kalimo, and B.A. Minassian. 2015. X-linked myopathy with excessive autophagy: a failure of self-eating. *Acta Neuropathol.* 129:383–390. https://doi.org/10.1007/s00401-015-1393-4

Funderburk, S.F., Q.J. Wang, and Z. Yue. 2010. The Beclin 1-VPS34 complex--at the crossroads of autophagy and beyond. *Trends Cell Biol.* 20:355–362. https://doi.org/10.1016/j.tcb.2010.03.002

Galluzzi, L., E.H. Baehrecke, A. Ballabio, P. Boya, J.M. Bravo-San Pedro, F. Cecconi, A.M. Choi, C.T. Chu, P. Codogno, M.I. Colombo, et al. 2017. Molecular definitions of autophagy and related processes. *EMBO J.* 36: 1811–1836. https://doi.org/10.15252/embj.201796697

Gillooly, D.J., I.C. Morrow, M. Lindsay, R. Gould, N.J. Bryant, J.M. Gaullier, R.G. Parton, and H. Stenmark. 2000. Localization of phosphatidylinositol 3-phosphate in yeast and mammalian cells. *EMBO J.* 19:4577–4588. https://doi.org/10.1093/emboj/19.17.4577

Golic, K.G., and S. Lindquist. 1989. The FLP recombinase of yeast catalyzes site-specific recombination in the Drosophila genome. *Cell.* 59:499–509. https://doi.org/10.1016/0092-8674(89)90033-0

Guo, L., C. Martens, D. Bruno, S.F. Porcella, H. Yamane, S.M. Caucheteux, J. Zhu, and W.E. Paul. 2013. Lipid phosphatases identified by screening a mouse phosphatase shRNA library regulate T-cell differentiation and protein kinase B AKT signaling. *Proc. Natl. Acad. Sci. USA.* 110: E1849–E1856. https://doi.org/10.1073/pnas.1305070110

Hasegawa, J., R. Iwamoto, T. Otomo, A. Nezu, M. Hamasaki, and T. Yoshimori. 2016. Autophagosome-lysosome fusion in neurons requires INPP5E, a protein associated with Joubert syndrome. *EMBO J.* 35:1853–1867. https://doi.org/10.15252/embj.201593148

Hasegawa, J., B.S. Strunk, and L.S. Weisman. 2017. PI5P and PI(3,5)P_2: Minor, but Essential Phosphoinositides. *Cell Struct. Funct.* 42:49–60. https://doi.org/10.1247/csf.17003

Holman, S.K., T. Morgan, G. Baujat, V. Cormier-Daire, T.J. Cho, M. Lees, J. Samanich, D. Tapon, H.D. Hove, A. Hing, et al. 2013. Osteopathia striata congenita with cranial sclerosis and intellectual disability due to contiguous gene deletions involving the WTX locus. *Clin. Genet.* 83:251–256. https://doi.org/10.1111/j.1399-0004.2012.01905.x

Hotta, K., T. Kitamoto, A. Kitamoto, S. Mizusawa, T. Matsuo, Y. Nakata, S. Kamohara, N. Miyatake, K. Kotani, R. Komatsu, et al. 2011. Association of variations in the FTO, SCG3 and MTMR9 genes with metabolic syndrome in a Japanese population. *J. Hum. Genet.* 56:647–651. https://doi.org/10.1038/jhg.2011.74

Itakura, E., C. Kishi-Itakura, and N. Mizushima. 2012. The hairpin-type tail-anchored SNARE syntaxin 17 targets to autophagosomes for fusion with endosomes/lysosomes. *Cell.* 151:1256–1269. https://doi.org/10.1016/j.cell.2012.11.001

Iyer, S., S. Suresh, D. Guo, K. Daman, J.C.J. Chen, P. Liu, M. Zieger, K. Luk, B.P. Roscoe, C. Mueller, et al. 2019. Precise therapeutic gene correction by a simple nuclease-induced double-stranded break. *Nature.* 568:561–565. https://doi.org/10.1038/s41586-019-1076-8

Jeschke, A., and A. Haas. 2016. Deciphering the roles of phosphoinositide lipids in phagolysosome biogenesis. *Commun. Integr. Biol.* 9. e1174798. https://doi.org/10.1080/19420889.2016.1174798

Juhász, G., J.H. Hill, Y. Yan, M. Sass, E.H. Baehrecke, J.M. Backer, and T.P. Neufeld. 2008. The class III PI(3)K Vps34 promotes autophagy and endocytosis but not TOR signaling in *Drosophila*. *J. Cell Biol.* 181:655–666. https://doi.org/10.1083/jcb.200712051

Ketel, K., M. Krauss, A.-S. Nicot, D. Puchkov, M. Wieffer, R. Müller, D. Subramanian, C. Schultz, J. Laporte, and V. Haucke. 2016. A phosphoinositide conversion mechanism for exit from endosomes. *Nature.* 529: 408–412. https://doi.org/10.1038/nature16516

Kim, G.H.E., R.M. Dayam, A. Prashar, M. Terebiznik, and R.J. Botelho. 2014. PIKfyve inhibition interferes with phagosome and endosome maturation in macrophages. *Traffic.* 15:1143–1163. https://doi.org/10.1111/tra.12199

Lee, T.V., H.E. Kamber Kaya, R. Simin, E.H. Baehrecke, and A. Bergmann. 2016. The initiator caspase Dronc is subject of enhanced autophagy upon proteasome impairment in Drosophila. *Cell Death Differ.* 23: 1555–1564. https://doi.org/10.1038/cdd.2016.40

Levin, R., S. Grinstein, and D. Schlam. 2015. Phosphoinositides in phagocytosis and macropinocytosis. *Biochim. Biophys. Acta.* 1851:805–823. https://doi.org/10.1016/j.bbalip.2014.09.005

Levine, B., and G. Kroemer. 2019. Biological Functions of Autophagy Genes: A Disease Perspective. *Cell.* 176:11–42. https://doi.org/10.1016/j.cell.2018.09.048

Liu, G.Y., and D.M. Sabatini. 2020. mTOR at the nexus of nutrition, growth, ageing and disease. *Nat. Rev. Mol. Cell Biol.* 21:183–203. https://doi.org/10.1038/s41580-019-0199-y

Lorenzo, O., S. Urbé, and M.J. Clague. 2006. Systematic analysis of myotubularins: heteromeric interactions, subcellular localisation and endosome related functions. *J. Cell Sci.* 119:2953–2959. https://doi.org/10.1242/jcs.03040

Lystad, A.H., and A. Simonsen. 2016. Phosphoinositide-binding proteins in autophagy. *FEBS Lett.* 590:2454–2468. https://doi.org/10.1002/1873-3468.12286

Maekawa, M., S. Terasaka, Y. Mochizuki, K. Kawai, Y. Ikeda, N. Araki, E.Y. Skolnik, T. Taguchi, and H. Arai. 2014. Sequential breakdown of 3-phosphorylated phosphoinositides is essential for the completion of macropinocytosis. *Proc. Natl. Acad. Sci. USA.* 111:E978–E987. https://doi.org/10.1073/pnas.1311029111

Mei, J., Z. Li, and J.F. Gui. 2009. Cooperation of Mtmr8 with PI3K regulates actin filament modeling and muscle development in zebrafish. *PLoS One.* 4. e4979. https://doi.org/10.1371/journal.pone.0004979

Mei, J., S. Liu, Z. Li, and J.F. Gui. 2010. Mtmr8 is essential for vasculature development in zebrafish embryos. *BMC Dev. Biol.* 10:96. https://doi.org/10.1186/1471-213X-10-96

Mulakkal, N.C., P. Nagy, S. Takats, R. Tusco, G. Juhász, and I.P. Nezis. 2014. Autophagy in Drosophila: from historical studies to current knowledge. *BioMed Res. Int.* 2014. 273473. https://doi.org/10.1155/2014/273473

Napolitano, G., and A. Ballabio. 2016. TFEB at a glance. *J. Cell Sci.* 129: 2475–2481. https://doi.org/10.1242/jcs.146365

Neukomm, L.J., A.-S. Nicot, J.M. Kinchen, J. Almendinger, S.M. Pinto, S. Zeng, K. Doukoumetzidis, H. Tronchère, B. Payrastre, J.F. Laporte, et al. 2011. The phosphoinositide phosphatase MTM-1 regulates apoptotic cell corpse clearance through CED-5-CED-12 in C. elegans. *Development.* 138: 2003–2014. https://doi.org/10.1242/dev.060012

Nicot, A.S., and J. Laporte. 2008. Endosomal phosphoinositides and human diseases. *Traffic.* 9:1240–1249. https://doi.org/10.1111/j.1600-0854.2008.00754.x

Palmieri, M., R. Pal, H.R. Nelvagal, P. Lotfi, G.R. Stinnett, M.L. Seymour, A. Chaudhury, L. Bajaj, V.V. Bondar, L. Bremner, et al. 2017. mTORC1-independent TFEB activation via Akt inhibition promotes cellular clearance in neurodegenerative storage diseases. *Nat. Commun.* 8:14338. https://doi.org/10.1038/ncomms14338

Raess, M.A., S. Friant, B.S. Cowling, and J. Laporte. 2017. WANTED - Dead or alive: Myotubularins, a large disease-associated protein family. *Adv Biol Regul.* 63:49–58. https://doi.org/10.1016/j.jbior.2016.09.001

Robinson, F.L., and J.E. Dixon. 2006. Myotubularin phosphatases: policing 3-phosphoinositides. *Trends Cell Biol.* 16:403–412. https://doi.org/10.1016/j.tcb.2006.06.001

Rong, Y., M. Liu, L. Ma, W. Du, H. Zhang, Y. Tian, Z. Cao, Y. Li, H. Ren, C. Zhang, et al. 2012. Clathrin and phosphatidylinositol-4,5-bisphosphate regulate autophagic lysosome reformation. *Nat. Cell Biol.* 14:924–934. https://doi.org/10.1038/ncb2557

Rubinsztein, D.C., P. Codogno, and B. Levine. 2012. Autophagy modulation as a potential therapeutic target for diverse diseases. *Nat. Rev. Drug Discov.* 11:709–730. https://doi.org/10.1038/nrd3802

Sardiello, M., M. Palmieri, A. di Ronza, D.L. Medina, M. Valenza, V.A. Gennarino, C. Di Malta, F. Donaudy, V. Embrione, R.S. Polishchuk, et al. 2009. A gene network regulating lysosomal biogenesis and function. *Science.* 325:473–477. https://doi.org/10.1126/science.1174447

Schink, K.O., K.-W. Tan, and H. Stenmark. 2016. Phosphoinositides in Control of Membrane Dynamics. *Annu. Rev. Cell Dev. Biol.* 32:143–171. https://doi.org/10.1146/annurev-cellbio-111315-125349

Schnorrer, F., C. Schönbauer, C.C.H. Langer, G. Dietzl, M. Novatchkova, K. Schernhuber, M. Fellner, A. Azaryan, M. Radolf, A. Stark, et al. 2010. Systematic genetic analysis of muscle morphogenesis and function in Drosophila. *Nature.* 464:287–291. https://doi.org/10.1038/nature08799

Scott, R.C., O. Schuldiner, and T.P. Neufeld. 2004. Role and regulation of starvation-induced autophagy in the Drosophila fat body. *Dev. Cell.* 7:167–178. https://doi.org/10.1016/j.devcel.2004.07.009

Settembre, C., R. Zoncu, D.L. Medina, F. Vetrini, S. Erdin, S. Erdin, T. Huynh, M. Ferron, G. Karsenty, M.C. Vellard, et al. 2012. A lysosome-to-nucleus signalling mechanism senses and regulates the lysosome via mTOR and TFEB. *EMBO J.* 31:1095–1108. https://doi.org/10.1038/emboj.2012.32

Srivastava, S., Z. Li, L. Lin, G. Liu, K. Ko, W.A. Coetzee, and E.Y. Skolnik. 2005. The Phosphatidylinositol 3-Phosphate Phosphatase Myotubularin- Related Protein 6 (MTMR6) Is a Negative Regulator of the Ca 2+-Activated K+ Channel K Ca 3. 1. *Mol. Cell. Biol.* 25:3630–3638. https://doi.org/10.1128/MCB.25.9.3630-3638.2005

Srivastava, S., L. Di, O. Zhdanova, Z. Li, S. Vardhana, Q. Wan, Y. Yan, R. Varma, J. Backer, H. Wulff, et al. 2009. The class II phosphatidylinositol 3 kinase C2β is required for the activation of the K+ channel KCa3.1 and CD4 T-cells. *Mol. Biol. Cell.* 20:3783–3791. https://doi.org/10.1091/mbc.e09-05-0390

Stauffer, W., H. Sheng, and H.N. Lim. 2018. EzColocalization: An ImageJ plugin for visualizing and measuring colocalization in cells and organisms. *Sci. Rep.* 8:15764. https://doi.org/10.1038/s41598-018-33592-8

Stoka, V., V. Turk, and B. Turk. 2016. Lysosomal cathepsins and their regulation in aging and neurodegeneration. *Ageing Res. Rev.* 32:22–37. https://doi.org/10.1016/j.arr.2016.04.010

Takáts, S., P. Nagy, Á. Varga, K. Pircs, M. Kárpáti, K. Varga, A.L. Kovács, K. Hegedűs, and G. Juhász. 2013. Autophagosomal Syntaxin17-dependent lysosomal degradation maintains neuronal function in Drosophila. *J. Cell Biol.* 201:531–539. https://doi.org/10.1083/jcb.201211160

Tang, L., Y. Tong, H. Cao, S. Xie, Q. Yang, F. Zhang, Q. Zhu, L. Huang, Q. Lü, Y. Yang, et al. 2014. The MTMR9 rs2293855 polymorphism is associated with glucose tolerance, insulin secretion, insulin sensitivity and increased risk of prediabetes. *Gene.* 546:150–155. https://doi.org/10.1016/j.gene.2014.06.028

Theodosiou, N.A., and T. Xu. 1998. Use of FLP/FRT system to study Drosophila development. *Methods.* 14:355–365. https://doi.org/10.1006/meth.1998.0591

Thurmond, J., J.L. Goodman, V.B. Strelets, H. Attrill, L.S. Gramates, S.J. Marygold, B.B. Matthews, G. Millburn, G. Antonazzo, V. Trovisco, et al; FlyBase Consortium. 2019. FlyBase 2.0: the next generation. *Nucleic Acids Res.* 47(D1):D759–D765. https://doi.org/10.1093/nar/gky1003

Tsukada, M., and Y. Ohsumi. 1993. Isolation and characterization of autophagy-defective mutants of Saccharomyces cerevisiae. *FEBS Lett.* 333:169–174. https://doi.org/10.1016/0014-5793(93)80398-E

Velichkova, M., J. Juan, P. Kadandale, S. Jean, I. Ribeiro, V. Raman, C. Stefan, and A.A. Kiger. 2010. Drosophila Mtm and class II PI3K coregulate a PI(3)P pool with cortical and endolysosomal functions. *J. Cell Biol.* 190:407–425. https://doi.org/10.1083/jcb.200911020

Wallroth, A., and V. Haucke. 2018. Phosphoinositide conversion in endocytosis and the endolysosomal system. *J. Biol. Chem.* 293:1526–1535. https://doi.org/10.1074/jbc.R117.000629

Wang, H., H.Q. Sun, X. Zhu, L. Zhang, J. Albanesi, B. Levine, and H. Yin. 2015. GABARAPs regulate PI4P-dependent autophagosome:lysosome fusion. *Proc. Natl. Acad. Sci. USA.* 112:7015–7020. https://doi.org/10.1073/pnas.1507263112

Waugh, M.G. 2016. Chromosomal Instability and Phosphoinositide Pathway Gene Signatures in Glioblastoma Multiforme. *Mol. Neurobiol.* 53:621–630. https://doi.org/10.1007/s12035-014-9034-9

Weavers, H., I.R. Evans, P. Martin, and W. Wood. 2016. Corpse Engulfment Generates a Molecular Memory that Primes the Macrophage Inflammatory Response. *Cell.* 165:1658–1671. https://doi.org/10.1016/j.cell.2016.04.049

Weidner, P., M. Söhn, T. Gutting, T. Friedrich, T. Gaiser, J. Magdeburg, P. Kienle, H. Ruh, C. Hopf, H.M. Behrens, et al. 2016. Myotubularin-related protein 7 inhibits insulin signaling in colorectal cancer. *Oncotarget.* 7:50490–50506. https://doi.org/10.18632/oncotarget.10466

Wen, J.K., Y.T. Wang, C.C. Chan, C.W. Hsieh, H.M. Liao, C.C. Hung, and G.C. Chen. 2017. Atg9 antagonizes TOR signaling to regulate intestinal cell growth and epithelial homeostasis in *Drosophila*. *eLife.* 6. e29338. https://doi.org/10.7554/eLife.29338

Wucherpfennig, T., M. Wilsch-Bräuninger, and M. González-Gaitán. 2003. Role of *Drosophila* Rab5 during endosomal trafficking at the synapse and evoked neurotransmitter release. *J. Cell Biol.* 161:609–624. https://doi.org/10.1083/jcb.200211087

Xue, Y., H. Fares, B. Grant, Z. Li, A.M. Rose, S.G. Clark, and E.Y. Skolnik. 2003. Genetic analysis of the myotubularin family of phosphatases in Caenorhabditis elegans. *J. Biol. Chem.* 278:34380–34386. https://doi.org/10.1074/jbc.M303259200

Yanagiya, T., A. Tanabe, A. Iida, S. Saito, A. Sekine, A. Takahashi, T. Tsunoda, S. Kamohara, Y. Nakata, K. Kotani, et al. 2007. Association of single-nucleotide polymorphisms in MTMR9 gene with obesity. *Hum. Mol. Genet.* 16:3017–3026. https://doi.org/10.1093/hmg/ddm260

Yoshii, S.R., and N. Mizushima. 2017. Monitoring and measuring autophagy. *Int. J. Mol. Sci.* 18:1865. https://doi.org/10.3390/ijms18091865

Yu, L., C.K. McPhee, L. Zheng, G.A. Mardones, Y. Rong, J. Peng, N. Mi, Y. Zhao, Z. Liu, F. Wan, et al. 2010. Termination of autophagy and reformation of lysosomes regulated by mTOR. *Nature.* 465:942–946. https://doi.org/10.1038/nature09076

Yu, L., Y. Chen, and S.A. Tooze. 2018. Autophagy pathway: Cellular and molecular mechanisms. *Autophagy.* 14:207–215. https://doi.org/10.1080/15548627.2017.1378838

Zhang, H., and E.H. Baehrecke. 2015. Eaten alive: novel insights into autophagy from multicellular model systems. *Trends Cell Biol.* 25:376–387. https://doi.org/10.1016/j.tcb.2015.03.001

Zoncu, R., R.M. Perera, D.M. Balkin, M. Pirruccello, D. Toomre, and P. De Camilli. 2009. A phosphoinositide switch controls the maturation and signaling properties of APPL endosomes. *Cell.* 136:1110–1121. https://doi.org/10.1016/j.cell.2009.01.032

Zou, J., S.C. Chang, J. Marjanovic, and P.W. Majerus. 2009a. MTMR9 increases MTMR6 enzyme activity, stability, and role in apoptosis. *J. Biol. Chem.* 284:2064–2071. https://doi.org/10.1074/jbc.M804292200

Zou, W., Q. Lu, D. Zhao, W. Li, J. Mapes, Y. Xie, and X. Wang. 2009b. Caenorhabditis elegans myotubularin MTM-1 negatively regulates the engulfment of apoptotic cells. *PLoS Genet.* 5:e1000679. https://doi.org/10.1371/journal.pgen.1000679

Zou, J., P.W. Majerus, D.B. Wilson, A. Schrade, S.-C. Chang, and M.P. Wilson. 2012a. The role of myotubularin-related phosphatases in the control of autophagy and programmed cell death. *Adv. Biol. Regul.* 52:282–289. https://doi.org/10.1016/j.advenzreg.2011.10.001

Zou, J., C. Zhang, J. Marjanovic, M.V. Kisseleva, P.W. Majerus, and M.P. Wilson. 2012b. Myotubularin-related protein (MTMR) 9 determines the enzymatic activity, substrate specificity, and role in autophagy of MTMR8. *Proc. Natl. Acad. Sci. USA.* 109:9539–9544. https://doi.org/10.1073/pnas.1207021109

JCB

Supplemental material

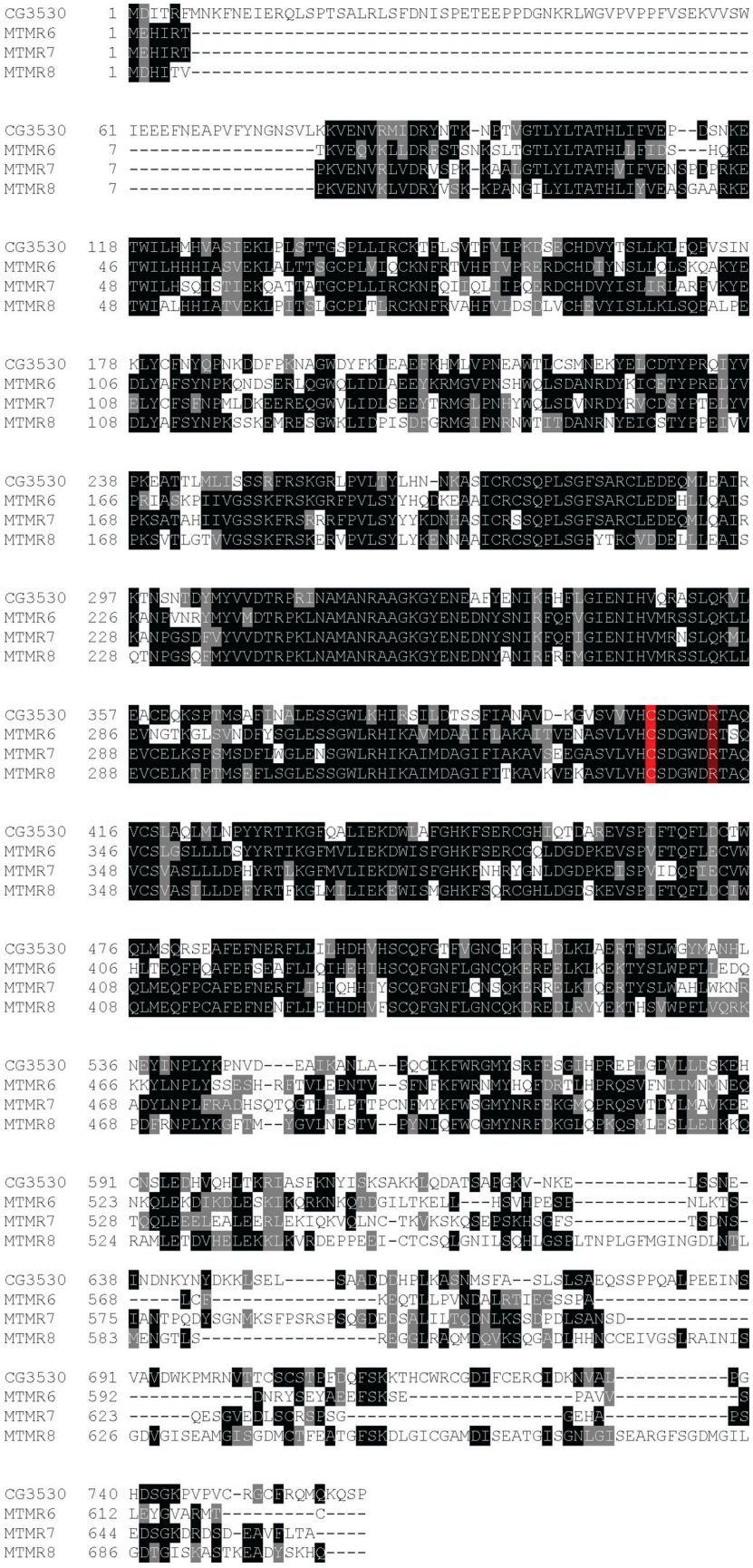

Figure S1. **Mammalian *MTMR6, MTMR7,* and *MTMR8* are *dMtmr6* orthologues.** Amino acid sequence alignment of the CG3530, MTMR6, MTMR7, and MTMR8. Conservation is shown as identical in black, similar in gray, and catalytic residues in red.

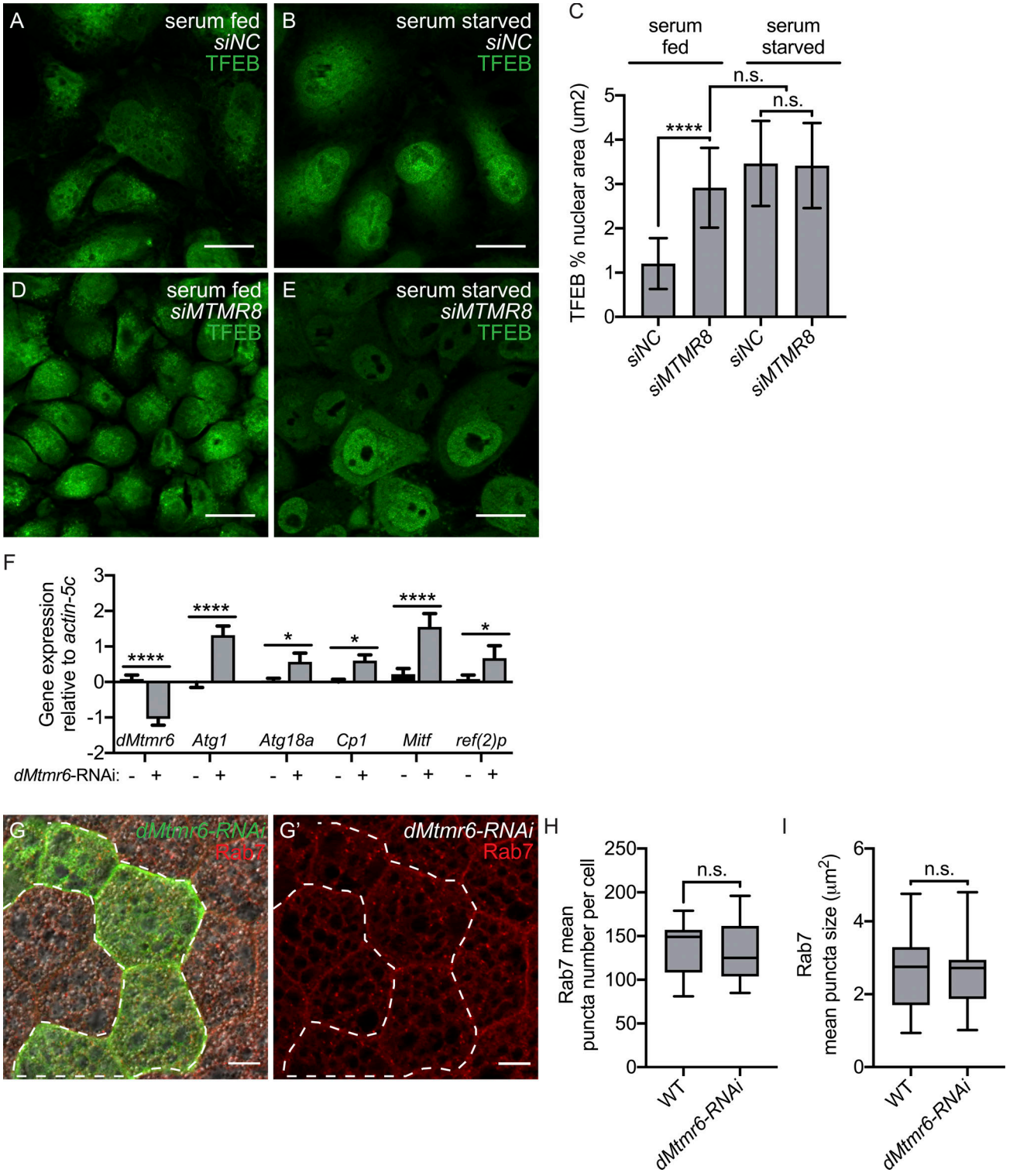

Figure S2. **dMtmr6 and MTMR8 maintain endolysosomal homeostasis. (A, B, D, and E)** Representative maximum intensity projection of z-stack image from serum-fed (A and D) or serum-starved (B and E) siRNA-transfected HeLa cells stained with antibodies to detect TFEB (green). **(C)** Quantification of nuclear TFEB in serum-fed and serum-starved HeLa cells transfected with the indicated siRNA as represented in A, B, D, and E. **(F)** Changes in transcription of known target genes of Mitf/TFEB relative to *actin-5c* in fat body from *Luciferase*-RNAi (–) or *dMtmr6*-RNAi (+) fat body–specific knockdown tissue. Please note that *Mitf* is the *Drosophila TFEB* orthologue, and *Cp1* is the gene for cathepsin L protein. **(G)** Representative image of fat body from fed L3 *Drosophila* larvae with WT (GFP-negative) and clonal d*Mtmr6*-knockdown cells (white dashed outline, green) stained with antibody to detect Rab7 (red) and Rab7 only channel depicted in G'. **(H and I)** Quantification of cellular Rab7 puncta number (H) and size (I) in WT control and *dMtmr6*-knockdown cells as represented in G. Data are presented as mean ± SD, *n* = 10 random images per genotype and condition (C); mean ± SD (*n* = 3 biological replicates; F); and mean ± minimum to maximum (*n* ≥ 11; H and I). Asterisks denote statistical significance (*, P < 0.05; ****, P < 0.0001) using one-way ANOVA (C), unpaired two-tailed *t* test in (F), and paired two-tailed *t* test (H, and I). Scale bars, 20 µm. n.s., not significant.

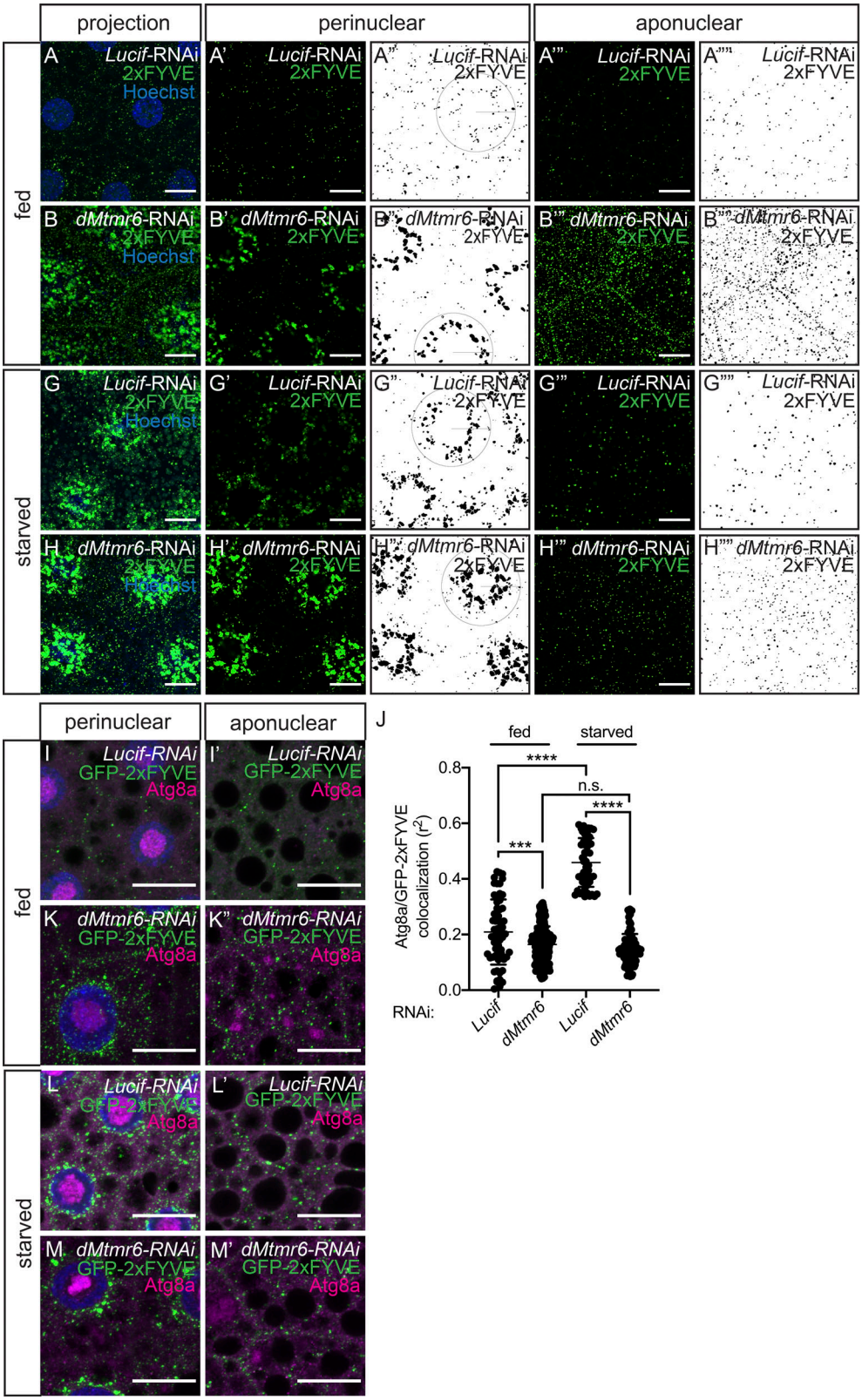

Figure S3. **dMtmr6 influences PI(3)P reporter distribution. (A, B, G, and H)** Representative images of indicated regions of Drosophila fat body overexpressing the PI(3)P reporter GFP-2xFYVE from fed (A and B) and starved animals (G and H). **(C–F)** Quantification of GFP-2xFYVE puncta from regions of interest as depicted in A″, B″, G″, and H″ (perinuclear) and A‴, B‴, G‴, and H‴ (aponuclear). **(I, K, L, and M)** Representative images of fed and starved *Drosophila* fat body overexpressing GFP-2xFYVE, stained with Hoechst to detect nuclei, and antibody stained to detect Atg8a. **(J)** Quantification of colocalization between GFP-2xFYVE and Atg8a as represented in I and K–M. Data are presented as mean ± minimum to maximum ($n \geq 10$; C–F and J). Asterisks denote statistical significance (*, $P < 0.05$; **, $P < 0.01$; ***, $P < 0.001$; ****, $P < 0.0001$), using one-way ANOVA. Scale bars, 20 μm. n.s., not significant.

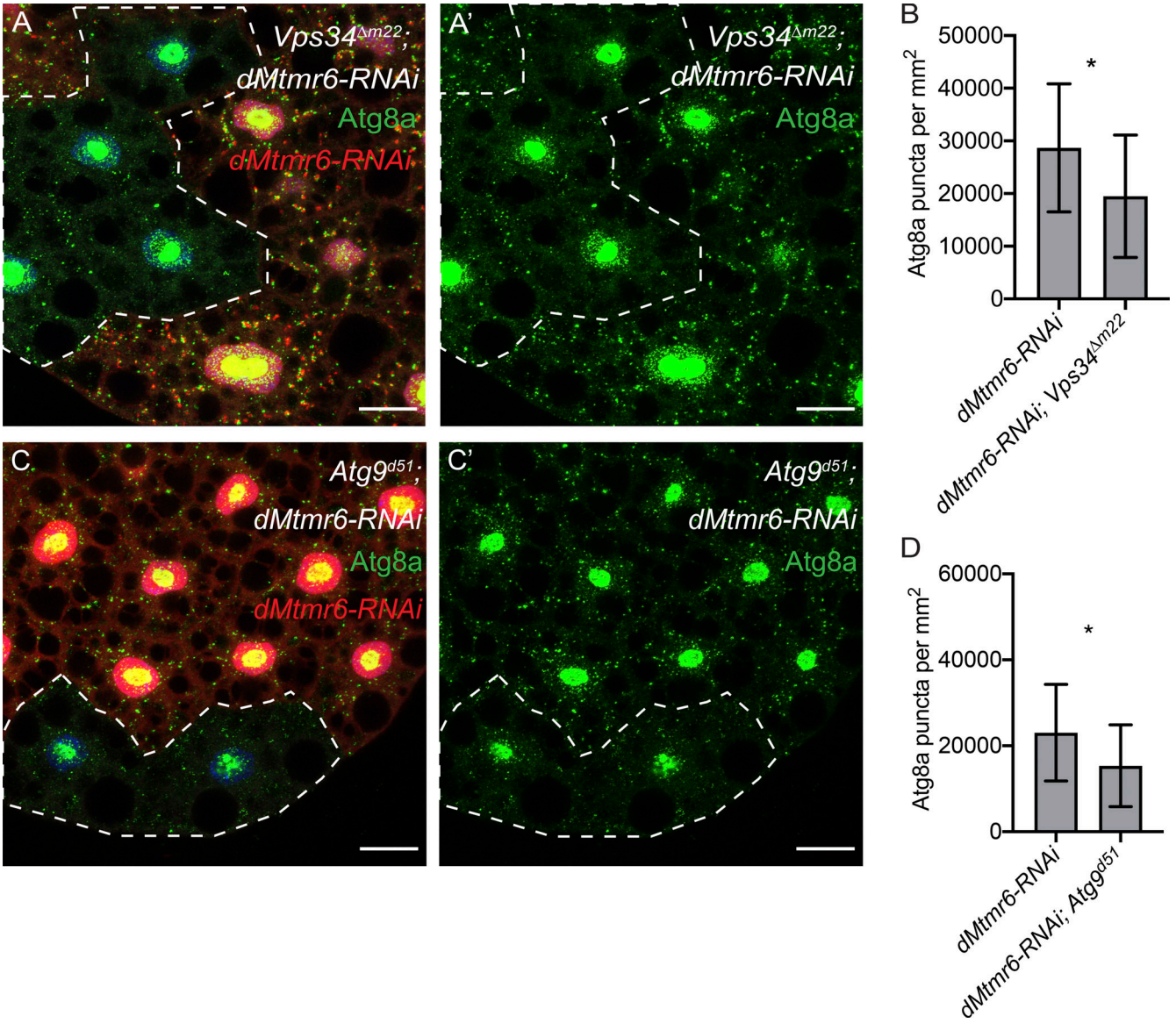

Figure S4. ***Vps34* and *Atg9* modify the *dMtmr6* autophagy phenotype. (A and C)** Representative images of fat body from starved L3 *Drosophila* larvae expressing *dMtmr6-RNAi* in which Vps34 (A) or Atg9 (C) homozygous mutant clones are induced (nondsRed, white dashed outline), stained with antibody to detect Atg8a, and staining for Atg8a only is depicted in A′ and C′. **(B and D)** Quantification of Atg8a puncta number as represented in (A and C). Data are presented as mean ± SD ($n \geq 9$; B and D). Asterisks denote statistical significance (*, $P < 0.05$), using unpaired two-tailed *t* test. Scale bars, 20 µm.

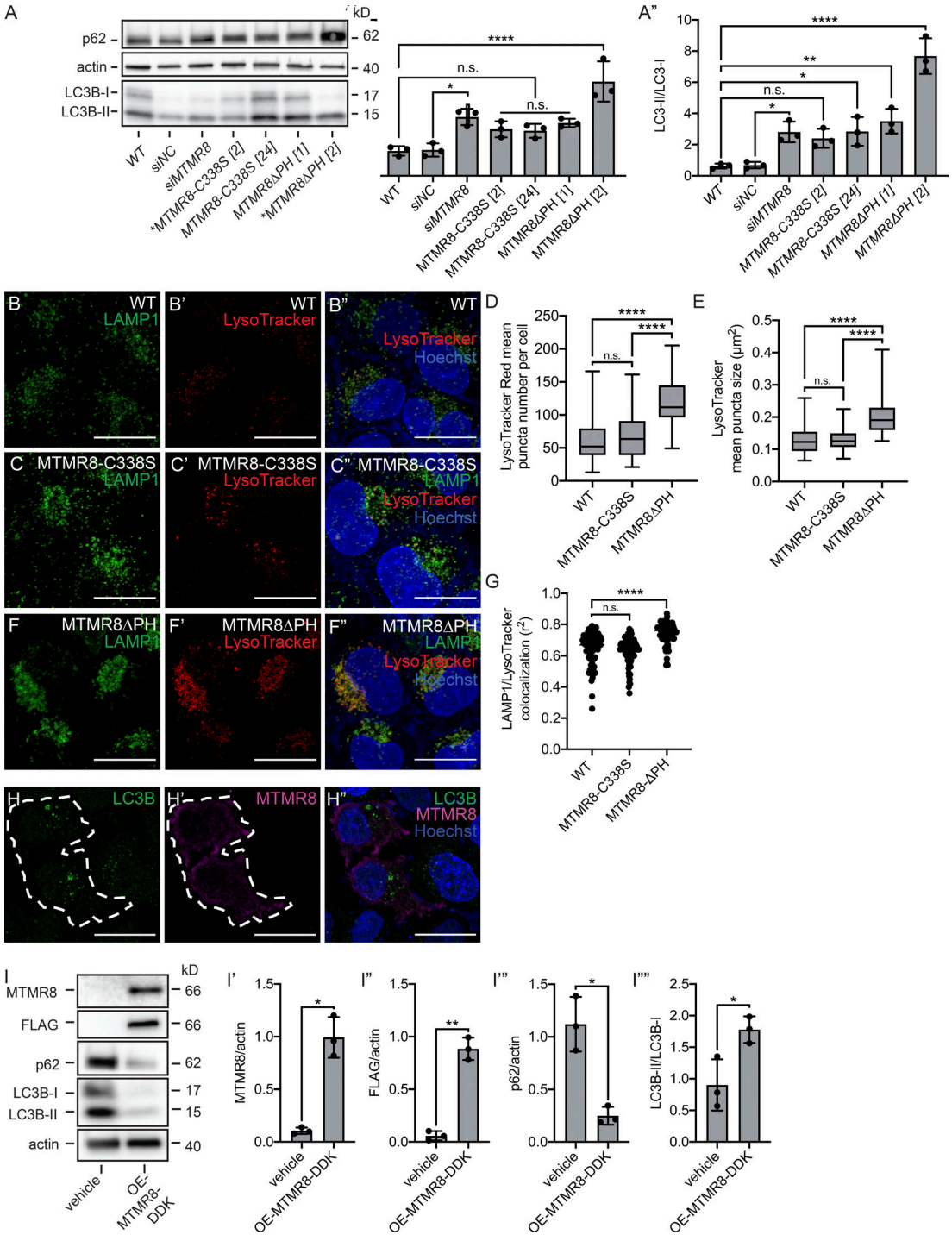

Figure S5. **Autolysosome homeostasis requires the MTMR8 PH-GRAM domain and catalytic cysteine residue. (A)** Representative Western blot from HeLa cells with the indicated genotypes to detect and quantify p62 relative to actin (A′) and lipidated LC3B-II relative to cytosolic LC3B-I (A″). Asterisks indicate cell lines used in images in B, C, and F and Fig. 8. **(B, C, and F)** Representative maximum intensity projection of z-stack image from HeLa cells with the indicated genotypes stained with Hoechst to detect nuclei (blue), LysoTracker to detect acidic vesicles (red, depicted in B′, C′, and F′, and merged in B″, C″, and F″), and antibody to detect LAMP1 (green, depicted in B, C, and F, and merged in B″, C″, and F″). Acidified lysosomal compartments contain both LAMP1 and LysoTracker. **(D and E)** Quantification of the number and size of cellular LysoTracker puncta as represented in B, C, and F. Please find LAMP1 quantifications in Fig. 8, D and F. **(G)** Quantification of LAMP1 and LysoTracker puncta colocalization as represented in B, C, and F. **(H)** Representative maximum intensity projection of z-stack image from HeLa cells transfected with *myc-DDK-MTMR8* and antibody stained with antibodies to detect LC3B (green, depicted in H as LC3B only, and merged in H″) and MTMR8 (magenta, white dashed line, depicted as MTMR8 only in H′, and merged in H″). **(I)** Representative Western blot from HeLa cells transfected with *myc-DDK-MTMR8* to detect MTMR8, DDK (FLAG), p62, and LC3B. Relative levels of protein are quantified as the ratio of MTMR8 to actin (I′), FLAG to actin (I″), p62 to actin (I′″), and LC3B-II to LC3B-I (I″″). Data are presented as mean in ± SD (n = 3; A and I) and mean ± minimum to maximum ($n \geq 5$ cells per 10 random images from three experimental replicates; D–G). Asterisks denote statistical significance (*, P < 0.05; **, P < 0.01; ****, P < 0.0001), using one-way ANOVA. Scale bars, 20 µm. n.s., not significant.

Provided online are two tables. Table S1 shows predicted *Drosophila* PI phosphatases based on FlyBase annotations, human orthologues, reagents tested, and results. Table S2 shows siRNA sequences used for cell culture experiments.